

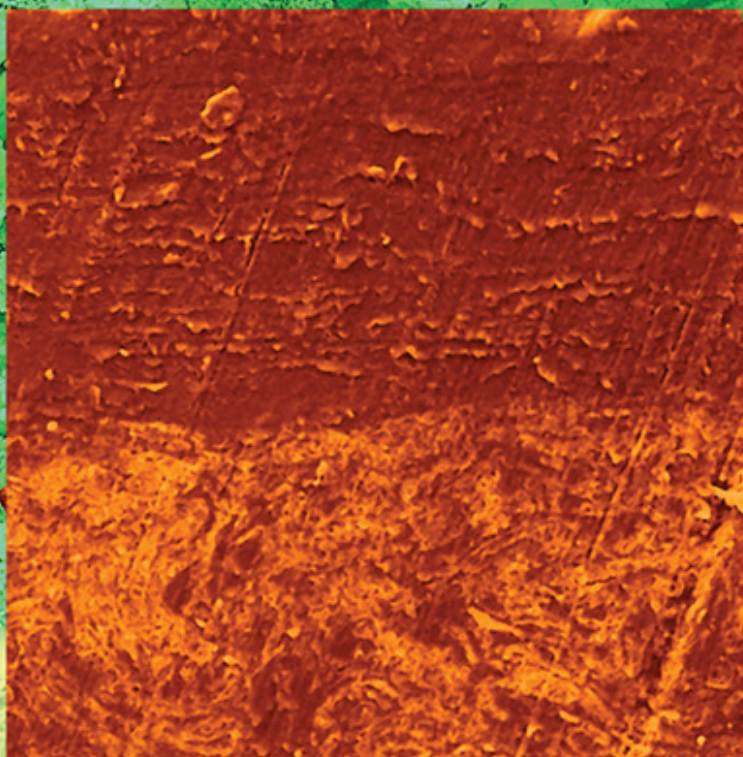
Volume 138 | Issues 21–22 | 2021

Included in this Print Edition:

Issue 21 (June 5, 2021)

Issue 22 (June 10, 2021)

JOURNAL OF  
**Applied Polymer**  
SCIENCE



WILEY

WILEYONLINELIBRARY.COM/APP



ARTICLE

# Polyetheretherketone, hexagonal boron nitride, and tungsten carbide cobalt chromium composite coatings: Mechanical and tribological properties

Janice L. Lebga-Nebane<sup>1,2</sup>  | Malavarayan Sankarasubramanian<sup>1,3,4</sup>  |  
Gregory Chojecki<sup>3,5</sup>  | Bo Ning<sup>6</sup> | Philip A. Yuya<sup>7</sup> | John C. Moosbrugger<sup>7</sup> |  
Don H. Rasmussen<sup>1</sup> | Sitaraman Krishnan<sup>1</sup> 

<sup>1</sup>Department of Chemical & Biomolecular Engineering, Clarkson University, Potsdam, New York, USA

<sup>2</sup>Presently at Elinor Coatings, Fargo, North Dakota, USA

<sup>3</sup>Materials Science & Engineering Ph.D. program, Clarkson University, Potsdam, New York, USA

<sup>4</sup>Presently at Intel Corporation, Chandler, Arizona, USA

<sup>5</sup>Presently at S-E-A Ltd., Columbus, Ohio, USA

<sup>6</sup>Oilfield Equipment Division, Baker Hughes, a GE Company, Houston, Texas, USA

<sup>7</sup>Department of Mechanical & Aeronautical Engineering, Clarkson University, Potsdam, New York, USA

## Correspondence

Sitaraman Krishnan, Department of Chemical & Biomolecular Engineering, Clarkson University, Potsdam, NY 13699, USA.

Email: skrishna@clarkson.edu

## Funding information

Clarkson University; General Electric

## Abstract

Composite powder coatings consisting of polyetheretherketone (PEEK), hexagonal boron nitride (hBN), and tungsten carbide cobalt chromium (WC-CoCr) particles were prepared by mechanical grinding and applied on steel substrates by thermal fusion of the thermoplastic polymer. The coatings contained about 20–60 vol% of hBN and WC-CoCr, and were designed to maximize modulus and hardness and minimize friction coefficient and wear rate. The mechanical and tribological properties of single- and double-layered coatings were characterized using nanoindentation and sliding friction and wear measurements. When the hBN concentration was about 30 vol%, the PEEK–hBN composite modulus was lower than that of neat PEEK, which is attributed to the disruption of PEEK crystallization by the filler particles. Upon the inclusion of WC-CoCr particles, the composite's modulus, and hardness showed a substantial increase beyond PEEK values. Elastic moduli of the mixed-filler systems were closer to the Reuss bound than the Voigt bound and could be correlated well with the coating composition using volume-fraction-weighted powers of component properties. Fitted values of the exponent (called the microstructural coefficient) were consistent with the expected continuity and connectivity of the composite's hard and soft phases. Viscoplastic energy dissipation increased with an increase in the polymer-filler interfacial area but decreased with the soft-phase volume fraction. The plasticity index was found to increase logarithmically with the coating modulus. The specific wear rate increased sharply beyond a composition-dependent critical value of the plasticity index. Mechanical polishing of the coating surfaces using abrasive slurries lowered the friction coefficient but increased the wear rate.

## KEYWORDS

composites, friction, mechanical properties, synthesis and processing techniques, thermoplastics, wear and lubrication

## 1 | INTRODUCTION

The relatively high levels of dissolved chlorides and other salts present in seawater make corrosion a significant problem for components, such as, gate valves in equipment used for seawater injection during oil and gas production. The surfaces of the valves must have a low coefficient of friction to provide lubricity during the opening and closing operations. They must be able to withstand high pressures, and they must have a high wear resistance. Hardfacing of the metallic surfaces using metal alloys is often used to improve wear resistance and extend the service life of the valve components,<sup>1</sup> but the resulting surfaces are prone to corrosion.<sup>2</sup> Corrosion is often a significant issue in metal matrix composites (wherein metal is the predominant component in the metal-ceramic composite coating). In fact, material failures in the offshore industry are often mainly due to corrosion rather than wear. While a low friction coefficient can be maintained by regular grease application, a long-term solution in the form of an intrinsically low-friction valve surface would be preferable. Diamond-like carbon (DLC) coatings possess several of the desirable properties, but the weak adhesion of DLC to steel alloys causes it to delaminate from the substrate, limiting its use.<sup>3</sup>

Polymer coatings can greatly alleviate seawater corrosion problems while providing surface lubricity that exceeds most metals and ceramics. Furthermore, their relatively straightforward processing and good adhesion to metallic substrates make them attractive for a variety of industrial applications. Poly(oxy-1,4-phenyleneoxy-1,4-phenylenecarbonyl-1,4-phenylene) (polyetheretherketone, PEEK) is a semicrystalline thermoplastic polymer (glass transition in the range of 140 to 175°C and melting in the range of 340 to 375°C) that is attractive for several engineering applications because of its remarkable thermochemical stability and mechanical properties.<sup>4–6</sup> The influence of the size and concentration of reinforcing filler particles, such as, alumina and silica on the tribological properties of PEEK composite coatings have been previously studied by various groups,<sup>7–12</sup> but the friction coefficients were relatively high, in the range of 0.30 to 0.55. Furthermore, depending on the chemical composition and microstructure of the particles, the wear performance of the PEEK composites can be adversely affected.<sup>13</sup> The addition of solid lubricants, such as, polytetrafluoroethylene (PTFE) and hexagonal boron nitride (hBN) in PEEK coatings lowers the friction coefficient of PEEK.<sup>14–19</sup> However, weakly adhesive additives, such as, PTFE adversely affect other desirable properties of PEEK, such as, modulus, hardness, and wear resistance. Therefore, tungsten carbide cermet particles were used as the second reinforcing filler in the present study, to not only

recover the mechanical properties of PEEK but also to enhance them. This article analyzes how the distribution of the two fillers across the cross-section of the coating affects its mechanical and tribological properties. A single-layered mixed filler system and a double-layered segregated filler system were studied.

Most previous studies in the literature on PEEK nanocomposite coatings focus on systems with a single type of functional filler at relatively low concentrations, generally < 10 vol%.<sup>7–11,19–20</sup> Particle aggregation adversely affected the mechanical properties of the composites at higher particle concentrations.<sup>19</sup> In contrast, the composite coatings of the present study contained a relatively soft but friction-reducing hexagonal boron nitride ceramic and a hard tungsten carbide cobalt chromium (WC-CoCr) cermet, at significantly higher concentrations (overall particle concentration ranging from 20 to 60 vol%), yet observing monotonic improvements in the coating modulus, hardness, and friction coefficient over this concentration range. To our knowledge, there are no reports on the combined influence of hexagonal boron nitride and tungsten carbide cobalt chromium on the mechanical and tribological properties of PEEK, necessitating further research of this interesting three-component system. This article provides some novel insights into previously unreported relationships between coating properties, such as, modulus, plasticity, and wear rate. It also presents an in-depth analysis of the effects of surface roughness on nanoindentation measurements of modulus and hardness.

The weak intermolecular forces of interaction that result in the desired surface lubricity (low friction coefficient) also weaken adhesive forces at the interface between the coating and the substrate. Therefore, the approach of using a base layer comprising of PEEK and WC-CoCr, to promote adhesion to steel and to increase coating hardness and stiffness, and a top layer comprising PEEK and hBN was evaluated. The effects of segregation of the two fillers into two different layers on the coating properties were investigated. The mechanical and tribological properties of the double-layered coatings were compared with single-layered coatings with the same overall composition. Polymer coating compositions that result in greatly enhanced properties for practical applications are reported.

## 2 | MATERIALS AND METHODS

### 2.1 | Composite powder preparation

PEEK (VICOTE 701, supplied by Victrex, Lancashire, UK, in the form of a powder with  $\cong 50 \mu\text{m}$  sized

particles), WC-CoCr (WC-760, Praxair Surface Technologies, Indianapolis, IN, WC 85 wt%, Co 10.5 wt%, and Cr 4.5 wt%, fine carbide grain size), hexagonal boron nitride (hBN, Industrial Supply, Twin Falls, ID) were used.

The composite powders were prepared by grinding the PEEK powder with the hBN and/or WC-CoCr powders in absolute ethanol (Pharmco-Aaper). A planetary ball mill (PQ-N2 Gear-Drive Planetary Ball Mill, Across International, Berkeley Heights, NJ), equipped with four 250-ml stainless steel jars and 6-mm (280 in number) and 10-mm (40) stainless steel balls, was used. The grinding of the particles in the slurry (50 g solids in 150 ml ethanol) was performed for 10 h, at 40 Hz and 500 rpm, changing rotating directions every 30 min. The particles settled out after the dispersions were allowed to stand overnight. The clear ethanol supernatant was decanted off. The wet mass of the settled solids was dried in an oven at 100°C and ambient pressure for about 1 h before further processing or characterization. Table 1 gives the compositions of the powders (and the coatings obtained using these powders).

Figure 1(a) is a photograph of a ball-milled composite powder, and Figure 1(b) is a scanning electron microscopy (SEM) image. Additionally, Figures S1 to S5 in Supporting Information show the SEM images of the as-received PEEK, hBN, and WC-CoCr powders, a ball-milled neat PEEK powder, and a ball-milled PEEK-hBN composite.

**TABLE 1** Concentrations of WC-CoCr, hBN, and PEEK in powders used to prepare the single-layered and double-layered composite coatings

	Weight percent			Density (g cm <sup>-3</sup> )
	PEEK	hBN	WC-CoCr	
Single-layered coating				
S40	60.0	20.0	20.0	1.77
S50	50.0	25.0	25.0	1.94
S65	35.0	32.5	32.5	2.25
Double-layered coating: the top layer				
D40	60.0	40.0	0.0	1.55
D50	50.0	50.0	0.0	1.62
D60	40.0	60.0	0.0	1.70
Double-layered coating: the bottom layer				
D40	60.0	0.0	40.0	2.07
D50	50.0	0.0	50.0	2.41
D60	40.0	0.0	60.0	2.89

## 2.2 | Composite coating preparation

The coatings were prepared by hot pressing the composite powders onto 2-mm thick 4130 alloy steel substrates at a temperature of 400°C using a compression molding press (Wabash MPI Carver, Model 25-1212-2TMB, Wabash, IN) and a steel mold shown in Figures 1(c) and 1(d). The procedure is described in Supporting Information. Figures 1(e) and 1(f) show photographs of steel substrates coated with the composite powder. Two types of coatings were studied: single-layered and double-layered structures. For preparing the double-layered coatings, a weighed amount of the powder of the desired bottom-layer composition (consisting of PEEK and WC-CoCr) was placed on the steel substrate and compacted in the mold at room temperature to achieve uniform coverage of the substrate. Then, the powder of the desired top-layer composition (consisting of PEEK and hBN) was applied uniformly on the compact bottom layer. The assembled double-layered green compact was hot-pressed at 400°C. In Table 1, the sample names of single-layered coatings are prefixed with "S" and those of the double-layered coatings with "D". The numbers in the sample names indicate the wt% of hBN and WC-CoCr.

The coatings were polished first using a water-based polycrystalline diamond suspension containing particles of 0.5 µm size (Allied High Tech Products Inc, Rancho Dominguez, CA) and a Billiard polishing cloth, and then with an aqueous dispersion of alumina particles of 0.05 µm diameter and a synthetic rayon cloth (MicroCloth, Buehler, Lake Bluff, IL). A Buehler Eco-Met III polisher (Buehler, Lake Bluff, IL) was used (cf. Supporting Information). Their surface roughness was determined using a TI-950 Triboindenter (Hysitron Inc., Minneapolis, MN) by carrying out "raster" scans using a Berkovich tip.

## 3 | CHARACTERIZATION METHODS

### 3.1 | Morphological characterization

Coating surface morphology and filler particle distribution within the polymer matrix were analyzed using JEOL 7400 high-resolution field emission scanning electron microscope coupled with an energy-dispersive X-ray spectroscopy (EDXS) detector. SEM analyses of cross-sections of the coatings were also carried out to determine the thickness of individual layers. The SEM specimens were prepared by cutting out coupons from the coated substrate using a diamond saw (12.7-mm Arbor IsoCut wafering blade, Buehler, Lake Bluff, IL). Figure 1



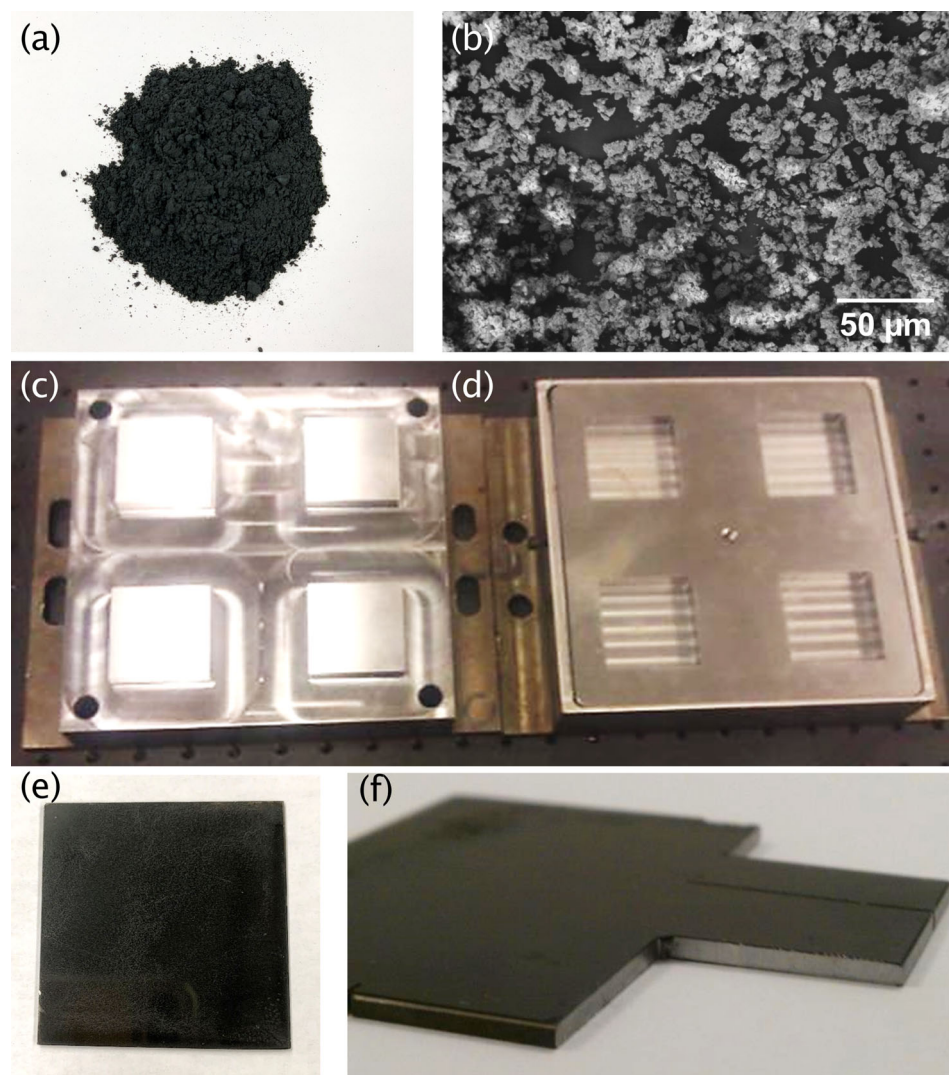


**FIGURE 1** (a) Photograph of a ball-milled powder coating composition containing PEEK, hBN, and WC-CoCr. (b) SEM image of the composite powder. (c and d) Steel mold consisting of four square wells that hold the  $5 \times 5$  cm steel substrates to be coated. Film thickness was controlled by the amount of polymer loaded into the mold. (e) Top view of a steel substrate coated with the PEEK/hBN/WC-CoCr composite. (f) Side-view of a coated steel substrate cut with a diamond saw, showing good adhesion of the coating to the substrate [Color figure can be viewed at [wileyonlinelibrary.com](http://wileyonlinelibrary.com)]

(f) shows a photograph of a substrate from which samples were cut. The coupon was mounted in a 25-mm diameter cylindrical epoxy mold such that the coating cross-section was exposed for SEM analysis. The epoxy mold assembly was polished using a series of sandpapers, starting from 200-grit and finishing with 1000-grit, to remove excess epoxy and obtain a smooth cross-section of the coated steel substrate for microscopy. Powder samples were sprinkled on double-sided adhesive carbon tapes attached to aluminum stubs. All SEM specimens were sputter-coated with a thin Au/Pd layer.

### 3.2 | X-ray diffraction

A Bruker D8 FOCUS diffractometer, equipped with a Ni foil filtered  $0.154 \text{ nm Cu K}\alpha$  X-ray source (2.2 kW Cu anode), a Bragg–Brentano theta-2theta geometry, and a scintillation counter detector, was used to generate the X-ray diffraction (XRD) patterns of the powders and the

coated substrates. For data acquisition, a scanning speed of  $0.05^\circ$  per second was used. The characterization was performed at room temperature. The XRD pattern of the uncoated steel substrate was also acquired. The XRD patterns of the coated substrates did not exhibit significant peaks corresponding to the underlying steel substrate.

### 3.3 | Nanoindentation

Nanoindentation measurements were performed using the TI-950 Triboindenter, wherein a load was continuously applied to the indenter, and the depth of penetration into the specimen was measured. A standard trapezoid load function was used with loading and unloading times set at 5 s and the holding time at 3 s. The applied loads ( $P_{\max}$  in Figure 2) ranged from 4 mN to a maximum of 10 mN with 0.25 mN increments (in load control). In general, 50 indentation measurements, involving two sets of sequential increase in  $P_{\max}$  from

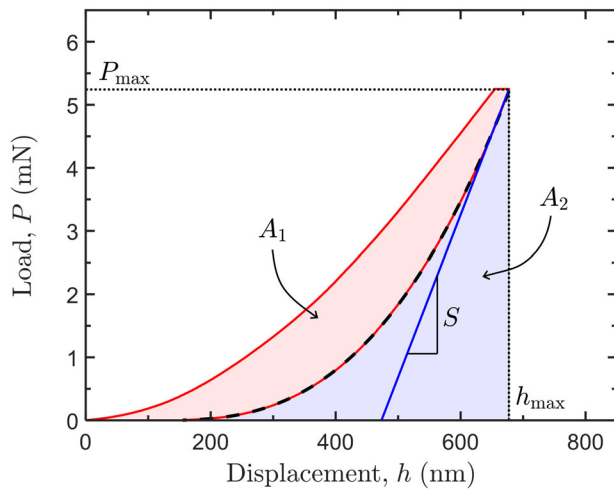


**FIGURE 2** Representative load vs. displacement data. The dashed curve is the best fit of the unloading section of the data to equation (1) [Color figure can be viewed at [wileyonlinelibrary.com](http://wileyonlinelibrary.com)]

4 to 10 mN, were made on each coating. All indents were on distinct points on the sample surface that were separated by a distance of 10  $\mu\text{m}$ . The data obtained from these experiments were analyzed using the standard procedure,<sup>21–22</sup> and statistical outliers were excluded.

The unloading portion of the load vs. displacement data were fitted to an empirical equation

$$P = A(h - h_f)^m \quad (1)$$

where  $A$ ,  $h_f$ , and  $m$  are fit parameters. The stiffness,  $S$ , is the slope of  $P$  vs.  $h$  at the maximum indentation depth,  $h_{\text{max}}$ :

$$S = \left. \frac{dP}{dh} \right|_{h=h_{\text{max}}} \quad (2)$$

The reduced modulus,  $E_r$ , is calculated from stiffness using:

$$E_r = \frac{S}{2} \sqrt{\frac{\pi}{A_c}} \quad (3)$$

where the contact area,  $A_c$ , is a function of the contact depth,  $h_c$ , defined as:

$$h_c = h_{\text{max}} - \frac{\epsilon P_{\text{max}}}{S} \quad (4)$$

For an ideal Berkovich tip,  $\epsilon = 0.75$  and  $A_c = 24.5h_c^2$ . The reduced modulus depends not only on the specimen modulus but also on the modulus of the diamond indenter.<sup>21–22</sup> Because the Young's modulus of the

indenter ( $\cong 1140$  GPa) is two orders of magnitude greater than that of the coatings tested, the reduced modulus and specimen modulus will differ only by an insignificant amount.

The hardness,  $H$ , defined as the material's resistance to plastic deformation under load, is related to the maximum applied load,  $P_{\text{max}}$ , by:

$$H = \frac{P_{\text{max}}}{A_c} \quad (5)$$

Plasticity index,  $\psi$ , which is used to quantify a material's viscoplasticity, was calculated using the areas,  $A_1$  and  $A_2$ , under the load–displacement plots, as shown in Figure 2 and Equation (6).

$$\psi = \frac{A_1}{A_1 + A_2} \quad (6)$$

$\psi = 0$  corresponds to a fully elastic behavior, and  $\psi = 1$ , completely plastic behavior.

### 3.4 | Tribology

Tribological tests were carried out using a commercial tribometer (BLR100, Bud Labs, Rochester, NY), equipped with a linear reciprocating ball-on-flat plane geometry, configured to measure the wear volume and the coefficient of kinetic friction of a flat surface in sliding contact with a spherical rider. A steel ball (52,100 alloy steel) of 6.35 mm diameter and hardness of 62 HRC was moved back and forth over the test surface under a normal force,  $W$ , of 1 kgf (9.8 N) at room temperature with no lubrication. Each test was performed at a speed of 5 cycles  $\text{s}^{-1}$  (300 rpm) and a stroke length,  $l$ , of 10 mm (in each direction), for 36 min (corresponding to  $n_{\text{cycles}} = 10,800$  cycles). The wear track was analyzed using stylus profilometry, in a direction perpendicular to the stroke length. Wear volume,  $V$ , was calculated as the product of the cross-sectional area of the wear track and the wear track length. The friction force was measured throughout the test and converted to a coefficient of friction. The specific wear rate,  $w_s$  ( $\text{mm}^3 \text{N}^{-1} \text{m}^{-1}$ ), was calculated using the Archard wear equation [Equation (7)]<sup>23</sup>:

$$w_s = \frac{V}{WL} \quad (7)$$

where the wear volume loss,  $V$ , is in  $\text{mm}^3$  and  $L$ , the total sliding distance, equal to  $2 \times l \times n_{\text{cycles}}$ , is in meters. The sliding speed, calculated from the stroke length and the number of cycles per second, was 0.1  $\text{m s}^{-1}$ .



## 4 | RESULTS AND DISCUSSION

### 4.1 | Coating composition

Table 1 shows the compositions of the composite powders and coatings of the present study. In each coating, the mass concentration of hBN was the same as that of WC-CoCr. The average density,  $\rho_c$ , of the composite was estimated using:

$$\rho_c = \frac{100}{\sum_i (C_i/\rho_i)} \quad (8)$$

where  $\rho_i$  is the density of component,  $i$  in the composite, and  $C_i$  is its concentration in wt%. In using Equation (8), it is assumed that the coatings prepared by compacting the composite powders at a temperature of 400°C, which is greater than the melting temperature of PEEK (343°C), have negligible porosity. The low porosity of the coatings is visually confirmed from their cross-sectional SEM images (vide infra). The volume percentage of PEEK, hBN, and WC-CoCr in the composite was calculated using their densities,  $\rho_p \cong 1.32 \text{ g/cm}^3$ ,  $\rho_{f,1} \cong 2.1 \text{ g/cm}^3$ , and  $\rho_{f,2} \cong 13.8 \text{ g/cm}^3$ , respectively (see Supporting Information), and Equation (9):

$$\phi_i = \left( \frac{C_i}{100} \right) \left( \frac{\rho_c}{\rho_i} \right) \quad (9)$$

where  $\phi_i$  is the volume fraction of component  $i$  in the composite.

Because of the large difference in the densities of hBN and WC-CoCr, the volume of hBN in the coating was  $\cong 6.6$  times higher than the WC-CoCr volume. The single-layered coatings consisted of both hBN and WC-CoCr throughout the coating volume. On the other hand, the double-layered coatings contained only hBN filled PEEK in the top layer, and only WC-CoCr filled PEEK in the bottom layer. The PEEK volume percent ranged from 59% to 81% in the single-layered coatings. It varied from 51% to 71% in the top layer and 87% to 94% in the bottom layer of the double-layered coatings. See Table S1 in Supporting Information for vol% concentrations.

A total filler concentration as high as 65 wt% yielded compact single-layered coatings with good cohesive strength between the filler particles and the matrix. However, it was not possible to obtain suitable double-layered coatings containing more than about 60 wt% of hBN in the top layer.

Table S2 (Supporting Information) gives selected physical properties of PEEK, hBN, and WC-CoCr. PEEK, hBN, and WC-CoCr have a modulus of 6.3, 20, and 590 GPa, respectively, and their hardness values are 0.39, 0.20, and 30 GPa, respectively.

### 4.2 | Surface and cross-sectional analyses of the PEEK composite coatings

SEM of the surfaces of the single- and double-layered coatings, shown in Figure S6 (of Supporting Information), indicate that the hot-pressing process used in this study resulted in compact films with a moderate degree of surface roughness. SEM images of the coating cross-sections are shown in Figure 3. Using cross-sectional SEM analysis, the thickness of the single-layered coatings was found to be in the range of 200–300  $\mu\text{m}$ , consistent with the thickness calculated using the composite density. SEM images of cross-sections of the double-layered coatings confirmed a layered architecture and were used to determine the individual layers' thickness. A clear distinction between the coating's base layer and the top layer was observed [see Figure 3(b)]. The double-layered coatings had an overall thickness of 400–500  $\mu\text{m}$ , and the top layers were 250–300  $\mu\text{m}$  thick.

The thickness of the compression-molded coatings, in  $\mu\text{m}$ , is related to the mass,  $m_c$  (g), and density,  $\rho_c$  ( $\text{g cm}^{-3}$ ), of the composite powder, and area,  $A_s$  ( $\text{cm}^2$ ), of the substrate according to:

$$t_c = \frac{m_c}{\rho_c A_s} \times 10^4 \quad (10)$$

The estimated density values for composites of different compositions are given in Table 1, using which the coating thicknesses could be calculated and found consistent with experimental observations.

The blending of the powder components using the ball-milling process was necessary to obtain uniform coatings. Figures S7 and S8 in Supporting Information show the energy-dispersive X-ray spectroscopy images of the surfaces of two different coatings: one prepared by compression molding of a blend of the as-received PEEK, hBN, and WC-CoCr powders obtained by manually shaking a mixture of the powders in a capped glass vial, and the other prepared using the ball-milled combination. A much more uniform distribution of hBN in the polymer matrix was observed when the ball-milled powder blend was used for preparing the coatings.

### 4.3 | X-ray diffraction analysis of composite powders and coatings

The crystallinity of PEEK in its coatings is known to have a substantial effect on its mechanical properties.<sup>24</sup> An XRD analysis was conducted to investigate the nature of the polymer in the composite coatings. Figure 4 shows the X-ray diffraction patterns of PEEK powder, WC-CoCr

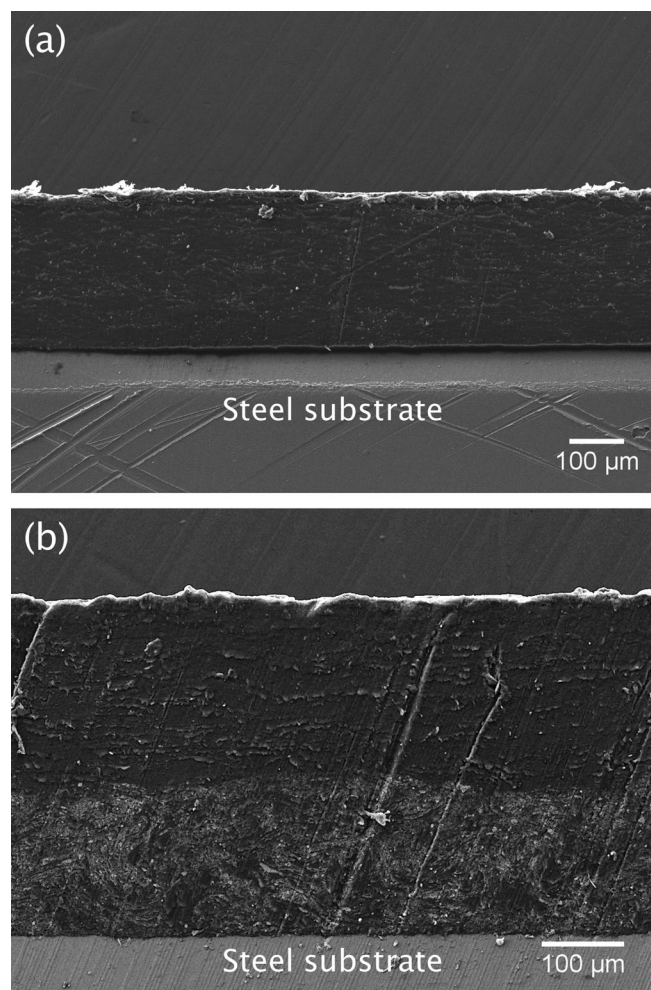


**FIGURE 3** SEM images of cross-sections of (a) S40 and (b) D60 coatings on steel. The top hBN/PEEK and bottom WC-CoCr/PEEK layers are seen in the image for D60

powder, hBN powder, the alloy steel 4130 substrate, a PEEK coating on the steel, and a representative monolayer coating consisting of PEEK, hBN, and WC-CoCr.

X-ray reflections from PEEK's orthorhombic unit cell<sup>25</sup> resulted in intensity peaks at  $2\theta$  angles of  $18.7^\circ$ ,  $20.6^\circ$ ,  $22.9^\circ$ , and  $28.8^\circ$  in the XRD pattern of the polymer. These  $2\theta$  peak positions correspond to reflections from the (110), (111), (200), and (211) planes, respectively.<sup>25–26</sup> Both the as-received powder and the compression-molded specimen of PEEK showed these peaks in their individual XRD patterns. However, the diffraction peaks were sharper (that is, their widths were narrower) for the compression-molded samples, indicating a higher degree of crystallinity because of the melting and slow crystallization of the chains during the molding process. Hedayati et al.<sup>27</sup> used XRD to analyze the crystallinity of powder composites of PEEK and silica nanoparticles surface-functionalized with 3-glycidoxypropyltrimethoxysilane prepared by ball milling. They found that the

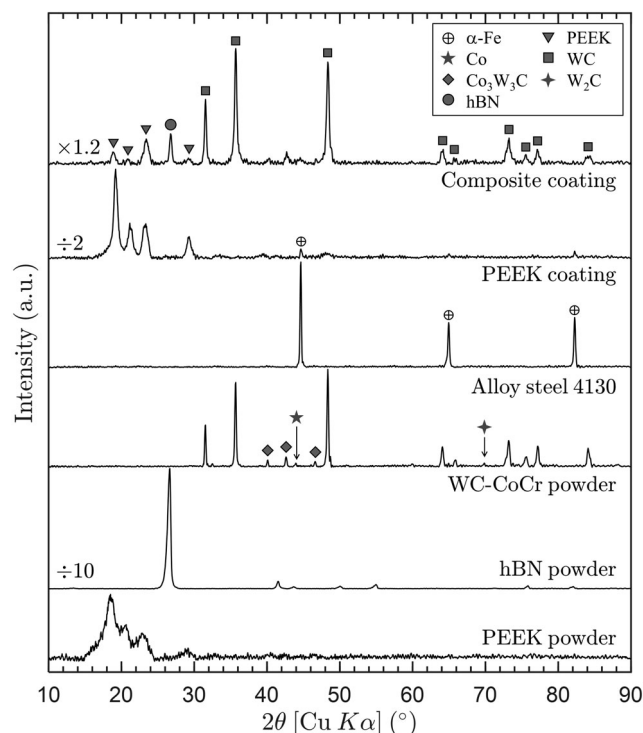


**FIGURE 4** X-ray diffractograms of the PEEK, hBN, and WC-CoCr raw materials (powders), the alloy steel substrate, and a representative composite coating (55 wt % PEEK, 22.5 wt % hBN, and 22.5 wt % WC-CoCr) on the steel substrate. XRD of the unpolished PEEK coating on the steel substrate is also shown

semicrystalline structure of PEEK was transformed into a completely amorphous structure during the early stages of ball milling and remained amorphous after that. However, the XRD pattern of the PEEK, hBN, and WC-CoCr composite coating of the present study did show the characteristic peaks of crystalline PEEK (see Figure 4), albeit of low intensity, attributed to some recrystallization of the polymer chains during compression molding.

hBN showed a diffraction peak at  $26.6^\circ$  due to diffraction by the (002) set of planes in the graphite-like structure of hBN.<sup>28</sup> The XRD pattern of the WC-CoCr cermet particles is discussed in Supporting Information. The alloy steel 4130 exhibited XRD peaks at  $44.5^\circ$ ,  $65.0^\circ$ , and  $82.3^\circ$  corresponding to (110), (002), and (121) reflections of  $\alpha$ -iron (ferrite) with a body-centered cubic structure.

#### 4.4 | Nanoindentation measurements of modulus, hardness, and plasticity index

Figure 5 shows load–displacement curves for a representative unpolished single-layered coating. The scatter in the plots indicates a distribution of surface stiffness (hardness) values.



In other words, the surface stiffness varied at different points on the surface, which is attributed to factors, such as, a variation in the local composition of PEEK, hBN, and/or WC-CoCr on the coating surface; the anisotropic mechanical properties of the hBN and WC-CoCr filler particles;<sup>29</sup> the differences in the mechanical properties of crystalline and amorphous domains of PEEK at the surface of the coatings;<sup>24</sup> and measurement artifacts introduced by surface roughness.

A similar scatter in the load–displacement plots was observed for unpolished (unfilled) PEEK coating as well (data not shown). Polishing the coatings' surfaces before nanoindentation measurements decreased the surface roughness and reduced the scatter in the load–displacement curves (and the  $E_r$  and hardness values calculated from these curves) to some extent.

Figure 6 shows the RMS and average roughness values of three single-layered coatings with different filler concentrations before and after polishing. The surface smoothness of the coatings significantly improved upon polishing. The RMS and average roughness values of the polished surfaces were all less than 80 nm, and the surfaces appeared visually shinier.

Figure 7 shows the reduced modulus obtained from the load–displacement measurements using different maximum indentation load,  $P_{\max}$ , at various points on the coating surface.

While there is no statistically significant variation of  $E_r$  with  $P_{\max}$  (which indicates that these measurements can extract information related to intrinsic material behavior reliably), a considerable scatter is

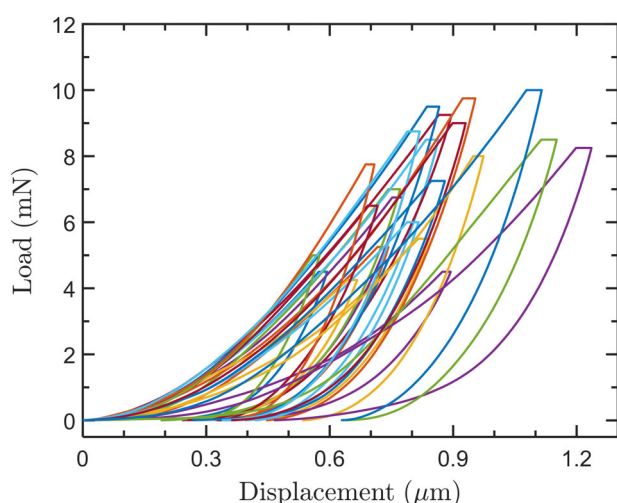


**FIGURE 5** Load–displacement curves from room temperature nanoindentation measurements on the single-layered coating, S65. These represent several cycles measured using a maximum load,  $P_{\max}$  (cf. Figure 2), varying from about 4 to 10 mN [Color figure can be viewed at [wileyonlinelibrary.com](http://wileyonlinelibrary.com)]

observed in individual  $E_r$  values about the mean because of the local surface heterogeneities. The distribution of  $E_r$  values could be fitted to a normal distribution, or a Burr distribution in some cases, as demonstrated in Figure 8 for the data from the measurements on the polished coatings PS65 and PS40 (polished single-layered coatings containing 65 and 40 wt % filler particles, respectively).

The probability density functions for these distributions are given by:

$$f_{\text{normal}}(x) = \frac{1}{\sigma\sqrt{2\pi}} \exp\left\{-\frac{(x-\bar{x})^2}{2\sigma^2}\right\} \quad (11)$$

and

$$f_{\text{Burr}}(x) = \frac{(kc/\alpha)(x/\alpha)^{c-1}}{[1 + (x/\alpha)^c]^{k+1}} \quad (12)$$

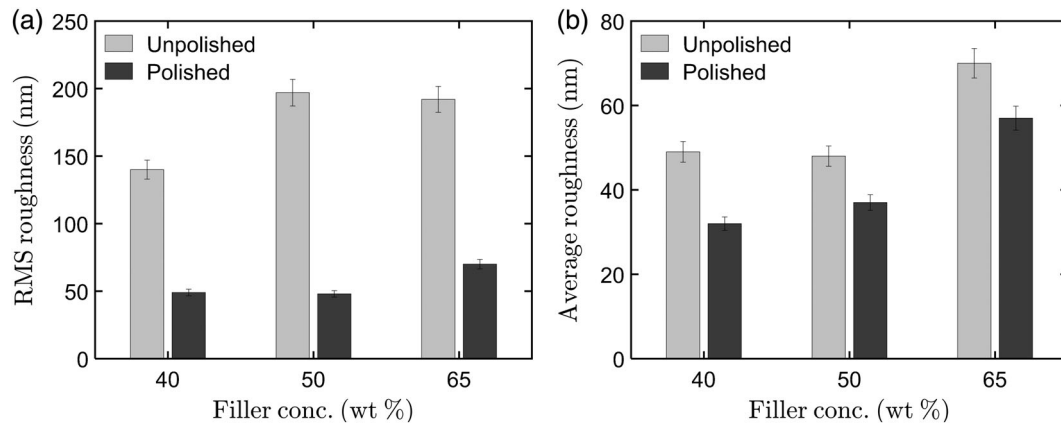
wherein  $\sigma$ ,  $\bar{x}$ ,  $k$ ,  $c$ , and  $\alpha$  are the parameters of the respective distributions. The probability plots shown in Figures 8(c) and 8(d) are seen to show good agreement with the experimental data.

Figure 9 shows the probability distribution plots of the reduced modulus values for three sets of coatings: Figure 9(a) shows the results for the unpolished single-layered coatings; Figure 9(b) shows the results for the corresponding polished coatings; the results for unpolished double-layered coatings are shown in Figure 9(c). The data for rough and polished PEEK coatings are also shown in this figure for comparison.

Except for the polished (unfilled) PEEK surface, which exhibited a narrow distribution of  $E_r$  centered around 6.3 GPa, all surfaces showed a relatively broad distribution of surface modulus values. The average reduced modulus of the unpolished PEEK coating was lower ( $\cong 5.1$  GPa). The narrower distribution and the higher value of the average modulus of the polished PEEK coating (compared with unpolished PEEK) point to the increased alignment of the polymer chains at the surface due to rubbing/polishing.<sup>30</sup>

#### 4.5 | Effect of filler concentration on the mechanical properties

For the single-layered coatings, the reduced modulus [Figure 10(a)] and the hardness [Figure 10(b)] increased with an increase in the concentration of the reinforcing filler. This increase was observed for both unpolished and polished surfaces.  $E_r$  of polished PEEK (unfilled) rose



**FIGURE 6** (a) Root-mean-squared roughness and (b) average roughness of unpolished coatings S40, S50, and S65, and polished coatings PS40, PS50, and PS65

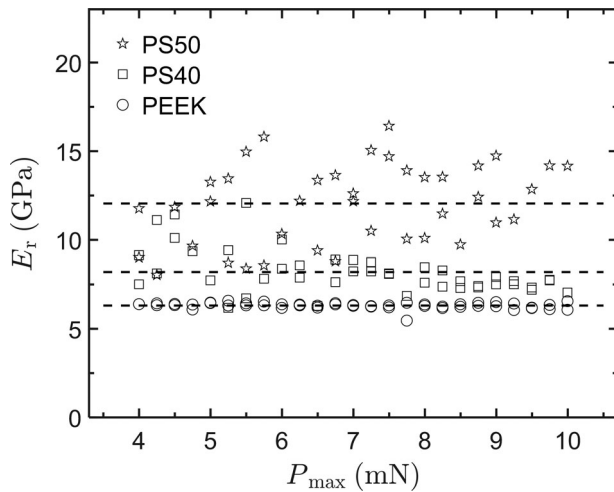


**FIGURE 7** Variation of reduced modulus of polished coatings with the maximum applied indentation load,  $P_{max}$

from about  $6.3 \pm 0.2$  to about  $17 \pm 3$  GPa when reinforced with WC-CoCr and hBN (65 wt% total concentration), and the hardness rose from about  $0.39 \pm 0.02$  to about  $0.69 \pm 0.12$  GPa.

In a tensile testing study of ball-milled PEEK–hBN nanocomposites prepared by compression molding, Liu et al.<sup>19</sup> reported an increase in the modulus from about 2.25 GPa for unfilled PEEK to a maximum of about 2.75 GPa for a composite containing 4 wt% hBN. A decrease in modulus was reported with a further increase in hBN concentration (2.63 GPa for 5 wt% hBN). Their hardness values were 0.285 GPa for unfilled PEEK and 0.381 GPa for PEEK filled with 5 wt% hBN. The significantly higher modulus and hardness values observed in the data of Figure 10 is attributed to the WC-CoCr, which is much stiffer and harder than hBN. Indeed, the modulus and hardness of the double-

layered coatings that contained only hBN in the top layer were much lower. For the coating D60 containing 60 wt% hBN in the top layer, these values were  $5 \pm 2$  and  $0.4 \pm 0.1$  GPa, respectively (cf. Figure 11).

Table 2 shows a comparison of the measured reduced modulus of the polished single-layered coatings with predictions using the volume fraction and elastic modulus of the individual components in the composite. The theoretical lower and upper bounds estimated using the Reuss and Voigt models,<sup>31</sup> and the empirical equation of Ji et al.<sup>32</sup> are shown along with the measured values.

In the Reuss series model, the different phases are under equal and uniform stress. In contrast, in the Voigt parallel model, the reinforcement and matrix are assumed to be under equal strain. These assumptions lead to Equation (13) for the elastic modulus of the series model

$$E_c = \frac{1}{\sum_{i=1}^N \phi_i / E_i} \quad (13)$$

and Equation (14) for that of the parallel model

$$E_c = \sum_{i=1}^N \phi_i E_i \quad (14)$$

In these equations,  $E_c$  is the elastic modulus of the composite,  $E_i$  is the modulus of phase  $i$  in the composite,  $\phi_i$  is the volume fraction of phase  $i$ , and  $N$  is the total number of phases. When the state of stress or strain is not uniform, the actual modulus is bounded by the values obtained using Equations (13) and (14).



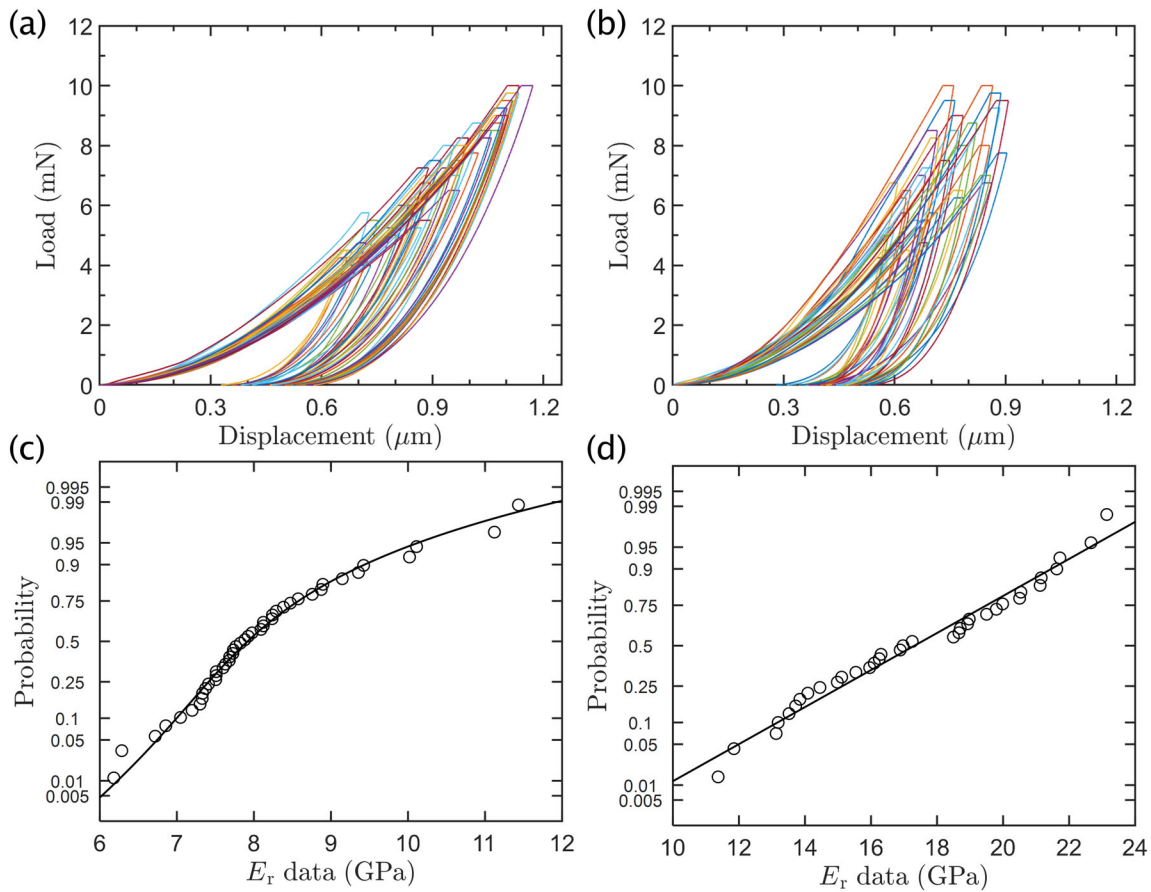


**FIGURE 8** Load–displacement curves for polished single-layered coatings PS40 (a) and PS65 (b). Probability plots for the reduced modulus values for PS40 (c) and PS65 (d) fitted to a Burr distribution and normal distribution, respectively. The lines in (c) and (d) are the best-fit curves [Color figure can be viewed at [wileyonlinelibrary.com](http://wileyonlinelibrary.com)]

$$\frac{1}{\sum_{i=1}^N \phi_i / E_i} \leq E_c \leq \sum_{i=1}^N \phi_i E_i \quad (15)$$

Equation (16) is an empirical model of Ji et al.,<sup>32</sup> where the composite property is obtained from the property value,  $P_i$ , of component  $i$  and  $J$  is a fitted parameter for a given system.

$$P_c = \left[ \sum_{i=1}^N \phi_i P_i^J \right]^{1/J} \quad (16)$$

Equations (13) and (14) are special cases of Equation (16).  $J = -1$  yields the harmonic mean or Reuss average [Equation (13)] and  $J = 1$  corresponds to the arithmetic mean or Voigt average [Equation (14)].  $J = 0$  yields the geometric mean.

In general, the parameter,  $J$ , referred to as a microstructural coefficient, depends on the shape and distribution of the hard and soft phases in a composite. Ji and co-workers found that  $J = 0.5$  gave good agreement with the experimental data of Young's modulus for the

composites in which soft spherical particles are isolated in a continuous hard matrix. In contrast, when hard spherical particles are dispersed in a continuous soft matrix,  $J = -0.5$ . If the dispersed phase particles are non-spherical,  $J = 0.25$  when the dispersed phase is soft, and  $J = -0.25$  when the dispersed phase is hard. When both the hard and soft phases are continuous,  $J$  values in the range of  $-0.5$  to  $0.5$  are expected.<sup>32</sup>

In the composites PS40, PS50, and PS65, the volume fraction of the PEEK soft phase is approximately 0.81, 0.73, and 0.60, respectively (Table S1). Except in the case of PS40, a common microstructural coefficient of 0.41 resulted in a good agreement between the measured and predicted  $E_r$  for multiple coatings. Conversely, a value of  $J$  can be found for each coating, which yields perfect agreement between the measured average  $E_r$  and the Ji et al. model. The last column of Table 2 shows these  $J$  values required to exactly match the measured  $E_r$ . The negative value of  $-0.228$  observed for PS40, with a soft continuous phase volume fraction of 0.81, is close to the expected value of  $-0.25$  for such systems. A microstructural coefficient of  $\cong 0.4$  for the other two composites,

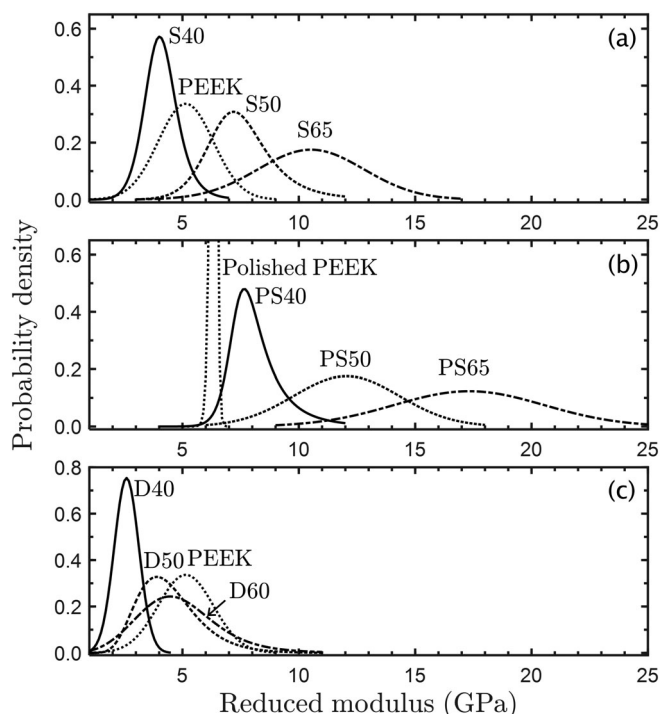


**FIGURE 9** Distribution of reduced modulus values for (a) unpolished single-layered coatings, S40, S50, and S65; (b) polished single-layered coatings, PS40, PS50, and PS65, and (c) unpolished double-layered coatings, D40, D50, and D60. The distributions for unpolished (a and c) and polished (b) unfilled PEEK coatings are also shown. The distribution of the reduced modulus values for the polished PEEK coating in (b) is relatively narrow and is shown truncated at the top

with lower volume fractions of PEEK, indicates a transitional structure in which both the hard (WC-CoCr and hBN) and soft (PEEK) phases are continuous in the loading direction.

Table 3 shows a similar comparison of the hardness values. The measured values are seen to be between the predicted lower and upper bounds and significantly closer to the Reuss lower bound than the Voigt upper bound. They show reasonable agreement with the empirical model of Ji et al.<sup>32</sup> for a fixed  $J$  value of  $\cong 0.49$ . An exact match with the measured hardness was possible with variable  $J$  values in the range of  $0.44 \pm 0.09$ . The models of Paul and Ishai–Cohen are discussed in Supporting Information. The Paul model resulted in a good fit of the experimental  $E_r$  data, but with an impractical estimate of the effective filler modulus.

#### 4.6 | Single-layered vs. double-layered coatings

The single-layered coatings S40 and S50 showed higher  $E_r$  and  $H$  than the double-layered coatings D40 and D50,

respectively, attributed to the fact that the single-layered coatings have the stiffer and harder WC-CoCr filler particles within the nanoindentation probe depth. The probe depth, (that is, the maximum indentation depth) in the nanoindentation studies of polymeric materials tends to range from 10 nm to 10  $\mu\text{m}$  for applied loads generally below 3 mN.<sup>33–35</sup> Because of the significant hardness of the filled PEEK coatings of the present study, the maximum indentation depth was below 2  $\mu\text{m}$  in spite of the relatively high indentation loads used ( $\cong 10$  mN). Thus, the probe depth was much smaller than the top layer's thickness in the double-layered coatings (which was in the range of 250–300  $\mu\text{m}$ ), and the measured properties are essentially those of the top layer, containing only hBN particles.

As seen in Figure 11(a),  $E_r$  and  $H$  of the double-layered coating D40 were lower than the corresponding values for unfilled PEEK. Evidently, the hBN filler particles in the top layer hinder the crystallization of PEEK, resulting in a decrease in the modulus. An increase in the hBN concentration to 50 and 60 wt% (in coatings D50 and D60, respectively) results in a partial recovery of the modulus and hardness values.

#### 4.7 | PEEK–hBN interfacial interactions

The thermodynamic work of adhesion,  $W$ , at the interface between two materials (the filler particles, F, and polymer matrix, P, in the present system) is given by:

$$W_{FP} = 2\sqrt{\gamma_F^d \gamma_P^d} + 2\sqrt{\gamma_F^p \gamma_P^p} \quad (17)$$

where  $\gamma^d$  and  $\gamma^p$  denote the dispersive and polar components of surface energy, respectively.<sup>36</sup> Given that the total surface energy,  $\gamma = \gamma^d + \gamma^p$ , Equation (17) can be written in the form

$$W_{FP} = \gamma_F + \gamma_P - \left( \sqrt{\gamma_F^d} - \sqrt{\gamma_P^d} \right)^2 - \left( \sqrt{\gamma_F^p} - \sqrt{\gamma_P^p} \right)^2 \quad (18)$$

from which it is seen that the work of adhesion increases with an increase in the total surface energy values of the filler and polymer ( $\gamma_F$  and  $\gamma_P$ , respectively), and with a decrease in the difference between the square roots of the individual components of surface energy [the third and the fourth terms on the right-hand side of Equation (18)].

The total surface energy of PEEK is relatively high, in the range of  $48 \pm 8$   $\text{mJ m}^{-2}$ , and its dispersive and polar components are  $43 \pm 5$  and  $5 \pm 3$   $\text{mJ m}^{-2}$ , respectively (see Supporting Information). Rathod and Hatzikiriakos,<sup>37</sup> who studied various grades of hBN with



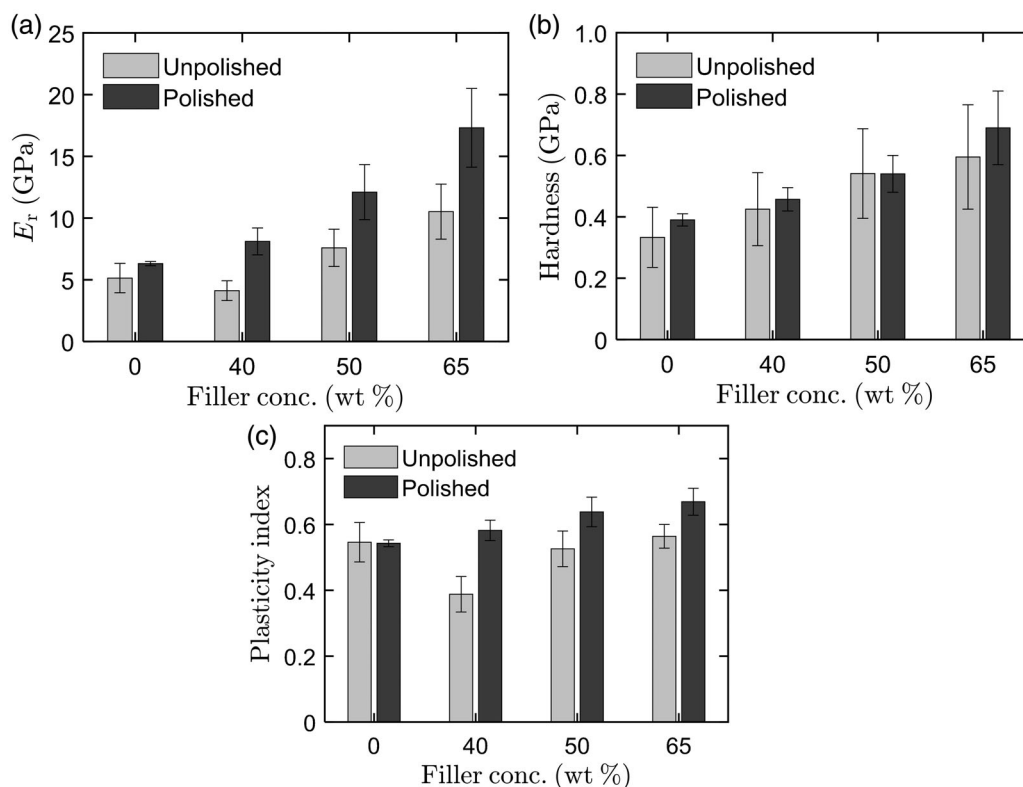


**FIGURE 10** (a) Reduced modulus, (b) hardness, and (c) plasticity index of unpolished and polished single-layer PEEK/WC-CoCr/hBN composite coatings with different filler concentrations. The error bars represent the standard deviations of the distributions

different particle sizes, aspect ratios, and boron oxide contents, reported that hBN has total surface energy in the range of 45 to 65  $\text{mJ m}^{-2}$ . The polar component of the hBN surface energy ranges from about 9 to about 29  $\text{mJ m}^{-2}$ , and the dispersive component is  $\cong 36 \text{ mJ m}^{-2}$  (almost the same for the different grades of hBN). Its surface energy is comparable to, or even higher than, some of the conventional fillers used in polymer nanocomposites.<sup>38</sup> Furthermore, using density functional theory calculations, Tsuji et al.<sup>39</sup> showed that there are acid–base interactions between the B atoms of hBN and O atoms of ethers and alcohols, and that the interfacial properties of hBN are fairly similar to those of graphite, which is known to disperse quite well in polymers.<sup>40</sup>

Thus, the PEEK–hBN interface would be sufficiently adhesive ( $W_{\text{FP}}$  in the range of  $95 \pm 25 \text{ mJ m}^{-2}$ ) to promote good bonding of hBN with PEEK. It is also clear that the surface lubricity of hBN-based composites is not because of low surface energy but because of the relative ease of the sliding of the honeycomb layers of boron nitride past each other in this two-dimensional material. Furthermore, the decrease in the modulus observed in Figure 11(a) upon the incorporation of 40 wt% hBN (even though hBN has a higher modulus than PEEK) must result from a decrease in the crystallinity of PEEK rather than the presence of any interfacial voids arising from

weak polymer–filler interfacial interactions. The X-ray diffractograms shown in Figure 4 indicate a decrease in PEEK crystallinity in the composite coating. A disproportionately large reduction in the intensity of the (110) reflection at  $2\theta \cong 18.7^\circ$  is seen in the composite coating (55 wt% PEEK) compared with the neat-PEEK coating (100 wt% PEEK).

#### 4.8 | Polished vs. unpolished coatings

Because of a high concentration of hBN in the top layer of the double-layered coatings, these coatings could not be polished effectively. The surface roughness increased after polishing by the formation of pits and crevices due to the flaking away of hBN layers from the coating surface. In contrast, all of the single-layered coatings, including S65 that contained the highest concentration of filler particles investigated, could be polished using the procedure developed in this study.

All the polished single-layered coatings exhibited higher modulus than the corresponding unpolished coatings, which is attributed to the removal of the polymer skin layer during polishing. A skin layer of PEEK is expected to be formed at the coating surface during the hot-pressing process (because  $\phi_{\text{PEEK}} > 0.50$  in each coating). The thinning or removal of

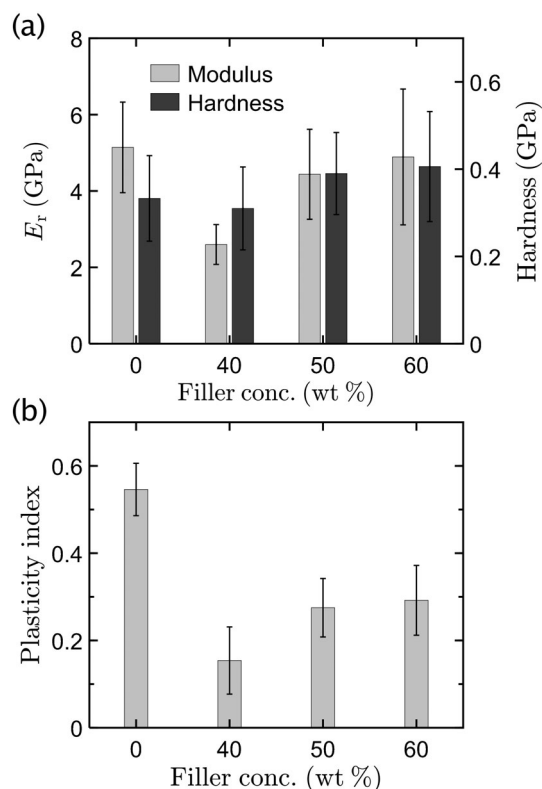


**FIGURE 11** (a) Reduced modulus and hardness, and (b) plasticity index of unpolished double-layer PEEK/WC-CoCr/hBN composite coatings with different filler concentrations. The error bars represent the standard deviations of the distributions

**TABLE 2** Reduced modulus,  $E_r$ , of polished single-layered coatings of different compositions measured using nanoindentation compared with the Reuss lower bound and Voigt upper bound and prediction using the model of Ji et al.<sup>32</sup>

	Measured <sup>a</sup>	Reuss	Voigt	Ji et al. <sup>b</sup>	$J^c$
PS40	8.1 (1.1)	7.35	23.6	10.70	-0.228
PS50	12.1 (2.2)	7.82	30.0	12.66	0.362
PS65	17.3 (3.2)	8.91	42.1	16.95	0.428

<sup>a</sup>Mean value; the numbers in parentheses is standard deviation.

<sup>b</sup>Fit parameter,  $J = 0.41$ .

<sup>c</sup>The value of  $J$  that results in exact agreement with measured  $E_r$ .

**TABLE 3** Hardness,  $H$ , of polished single-layered coatings of different compositions measured using nanoindentation compared with the Reuss lower bound and Voigt upper bound and prediction using the model of Ji et al.<sup>32</sup>

	Measured <sup>a</sup>	Reuss	Voigt	Ji et al. <sup>b</sup>	$J^c$
PS40	0.46 (0.04)	0.34	1.12	0.51	0.352
PS50	0.54 (0.06)	0.33	1.39	0.56	0.458
PS65	0.69 (0.12)	0.30	1.90	0.66	0.514

<sup>a</sup>Mean value; the numbers in parentheses is standard deviation.

<sup>b</sup>Fit parameter,  $J = 0.49$ .

<sup>c</sup>The value of  $J$  that results in exact agreement with measured hardness.

this layer by polishing results in a greater influence of the harder filler particles at the coating surface, increasing the average modulus and hardness.

#### 4.9 | Plasticity index

The plasticity index,  $\psi$ , of the coatings containing different filler concentrations was calculated using Equation (6) and found to be in the range of about 0.1 to about 0.7. It is a measure of the coating's propensity to undergo permanent deformation and release strain energy by viscous dissipation.<sup>22,40</sup> The variations of  $\psi$  with filler concentration are shown in Figure 10(c) for single-layered coatings and Figure 11(b) for double-layered coatings, wherein a general trend of increasing  $\psi$  with an increase in filler concentration is observed in the case of filled coatings.

The plasticity index of the polished single-layered coatings increased from  $0.54 \pm 0.01$  for unfilled PEEK to  $0.58 \pm 0.03$  for the PS40 coating that contained 40 wt% filler particles and  $0.67 \pm 0.04$  for the PS65 coating. The increase in  $\psi$  with an increase in the filler concentration is attributed to frictional dissipation of the work done during indentation at the filler-polymer interface. For a polymer composite in which the filler particles are uniformly dispersed (and are not aggregated), the filler-polymer interfacial area would increase with an increase in the concentration of the filler. Hence,  $\psi$  would increase with an increase in the filler concentration.

However, viscous dissipation of the indentation work within the PEEK matrix also appears to be significant in certain composites of the present study. The plasticity index of some of the composite coatings was found to be lower than that of unfilled PEEK polymer [e.g., compare  $\psi$  values for unpolished PEEK and S40 in Figure 10(c), and of the composites in Figure 11(b)]. A fraction of the total volume of the composite is occupied by stiff filler particles. The polymer volume in the region indented during the experiment is lower in a composite than that in neat PEEK. PEEK would have a greater ability to dissipate the work done during indentation toward plastic deformation than the significantly stiffer filler particles. Hence,  $\psi$ , which represents the fraction of indentation work that is not recovered due to viscous dissipation, is lower for some filled-PEEK samples.

The relative influence of these two effects—frictional dissipation at the filler-polymer interface and viscous dissipation in the form of plastic deformation of the PEEK matrix—would determine the overall plasticity index. Accordingly,  $\psi$  of many of the composite coatings were lower than that of unfilled PEEK polymer.

The plasticity index of the unpolished PEEK coating ( $0.54 \pm 0.01$ ) was fairly close to that of the polished

surface ( $0.55 \pm 0.06$ ). However, the  $\psi$  values for the unpolished composite coatings were somewhat lower than those of the polished surfaces [cf. Figure 10(c)]. For example,  $\psi$  was  $0.39 \pm 0.05$  for unpolished S40 and  $0.58 \pm 0.03$  polished PS40.

$\psi$  was the lowest for the double-layered coatings that contained PEEK–hBN composites at the surface.  $\psi$  increased from  $0.15 \pm 0.08$  for D40 to  $0.29 \pm 0.08$  for D60. These values were lower than the  $\psi$  of single-layered coatings ( $0.39 \pm 0.05$  and  $0.67 \pm 0.05$  for S40 and S65, respectively). The lower values are attributed to the lower volume fraction of PEEK in the top layer of the double-layered coatings compared with the single-layered coatings.  $\phi_{\text{PEEK}}$  is about 0.81 and 0.60 in S40 and S65, respectively, whereas it is 0.71 and 0.52 in D40 and D60, respectively. A lower volume fraction of the softer component (PEEK) results in lower plastic deformation. Additionally, the weaker intermolecular forces of interaction between PEEK and hBN (compared with PEEK and WC–CoCr), and between the hBN interlayers, would result in lower energy dissipation due to friction, and therefore, lower  $\psi$ .

$\psi$  was found to increase with an increase in  $E_r$ , indicating that the elastic recovery, after indentation, was lower for a stiffer surface, at least over the time scale of the nanoindentation experiments. For all sets of unpolished and polished composite coatings,  $\psi$  showed a nearly logarithmic correlation with  $E_r$ :

$$\psi \cong 0.29 \ln(E_r/1.4); (r^2 = 0.89) \quad (1)$$

A slightly higher value of regression coefficient could be obtained using a model of the form  $\psi = ae^{-b/E_r}$  where  $a$  and  $b$  are fit parameters (Figure 12). Regardless, it is interesting that the data for various coatings, polished and unpolished, assembled along the same curve.

#### 4.10 | Friction coefficient

The polished unfilled-PEEK coating exhibited a friction coefficient of 0.48. Figures 13(a), 13(b) show that the friction coefficients of the filled-PEEK coatings were significantly lower than that of PEEK. The friction coefficient decreased with an increase in the filler concentration, clearly due to the increased surface concentration of the hBN particles, which acted as a solid lubricant. The two-dimensional morphology of hBN would facilitate the sliding of hBN platelets relative to each other, lowering the frictional force at the interface. Furthermore, the relatively high thermal conductivity of hBN would also help reduce the frictional force.

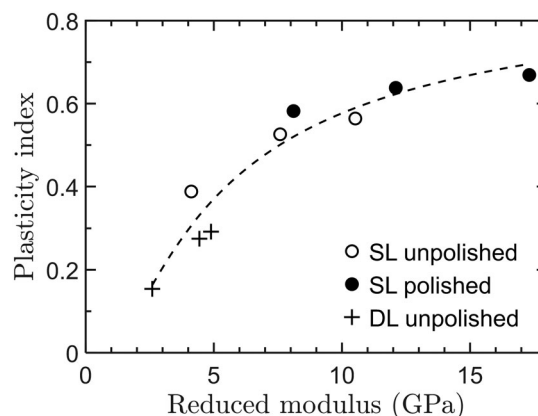


**FIGURE 12** Plastic index vs. reduced modulus for the various PEEK/hBN/WC–CoCr composite coatings of the present study. SL and DL denote single- and double-layered coatings, respectively. The dashed line is a fit of the experimental data to the empirical equation,  $y = ae^{-b/x}$ ;  $a = 0.9 \pm 0.2$ ,  $b = 4.4 \pm 1.4$ , and  $r^2 = 0.91$

Because of the low thermal conductivity of PEEK, the frictional heat generated during the sliding motion has been shown to raise the temperature at the interface.<sup>41–43</sup> King and Tabor found that the friction coefficient of thermoplastics such as poly(methyl methacrylate), polyethylene, and polychlorotrifluoroethylene (Kel-F), increased with an increase in temperature.<sup>44</sup> A similar increase in the friction coefficient of PEEK has been reported by Tharajak et al.<sup>18</sup> The hBN particles in the polymer matrix (that form a percolating network because of their high concentration) transfer heat away from the contact, lowering the friction coefficient.

The double-layered coatings B40 and B50 had lower friction coefficients (0.23 and 0.22, respectively) than the single-layered coatings S40 and S50 (0.25 and 0.24, respectively), which is attributed to the higher surface concentration of hBN in B40 and B50.

The polished single-layered coatings PS40 and PS65 showed lower friction coefficients than the unpolished coatings S40 and S65, respectively. The lowest friction coefficient observed in the present study was 0.21 for the unpolished D60 double-layered coating with the highest surface concentration of hBN (among the test samples discussed here).

#### 4.11 | Wear

Figures 13(c), 13(d), 14 show the specific wear rates,  $w_s$  [cf. Equation (7)], of the composite coatings of different compositions. The wear rates of the composite coatings of the present study were significantly higher than that of the polished unfilled PEEK coating, for which,  $w_s \cong 1.37 \times 10^{-5} \text{ mm}^3 \text{ N}^{-1} \text{ m}^{-1}$ .



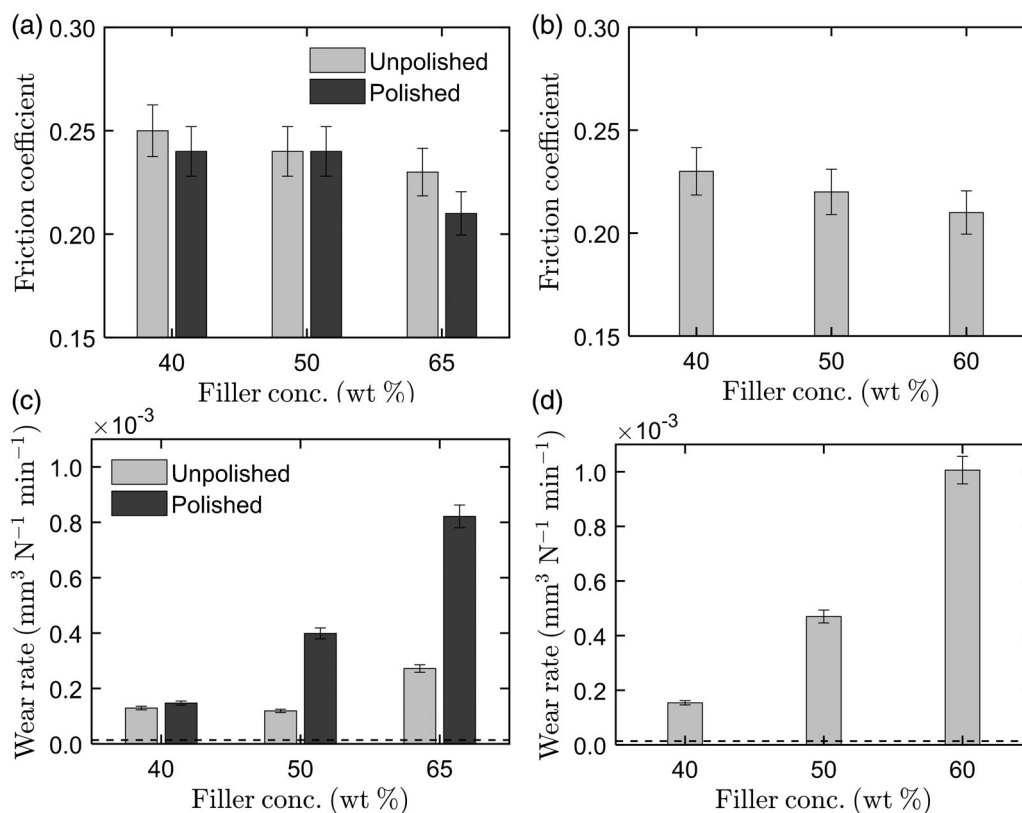


**FIGURE 13** The variation of friction coefficient (a, b) and specific wear rate (c, d) with filler concentration for single-layered coatings (a, c) and double-layered coatings (b, d). Measurements were at room temperature using a linearly reciprocating ball-on-flat arrangement with a 6.35 mm diameter steel ball, a normal force of 1 kgf, a sliding speed of  $0.1 \text{ m s}^{-1}$ , and a total sliding distance of 216 m. Error bars denote 5% uncertainty bounds. Dashed lines in (c) and (d) represent the baseline wear rate of neat PEEK ( $\approx 1.37 \times 10^{-5} \text{ mm}^3 \text{N}^{-1} \text{m}^{-1}$ )

The wear rate increased by almost one order of magnitude when the filler concentration increased over a range of 40 to 65 wt%. The formation of a transfer film of polymer on the steel rider would significantly lower friction coefficient and wear rate when the polymer is of low surface energy (e.g., PTFE) and when the sliding speed is low.<sup>45</sup> However, at the relatively high sliding speed of

$0.1 \text{ m s}^{-1}$  employed in the present study, subsurface crack propagation and the removal of large scale debris from the surface would be the primary mechanism of wear.<sup>46</sup>

The role of filler particles in such cases would be to hinder subsurface crack propagation. Stiffer filler particles would offer greater resistance to crack propagation than softer fillers. Thus, the unpolished single-layered coatings S50 and S65 that contained WC-CoCr particles at the contact surface (in addition to hBN particles) showed significantly lower wear rates [cf. Figure 13(c)] than the unpolished double-layered coatings D50 and D60 [cf. Figure 13(d)] that contained hBN particles in the top layer of the coating. The elastic modulus of S50 and S65 coatings were  $7.6 \pm 1.5 \text{ GPa}$  and  $10.5 \pm 2.2 \text{ GPa}$ , respectively, while those of D50 and D60 were  $4.4 \pm 1.2 \text{ GPa}$  and  $4.9 \pm 1.8 \text{ GPa}$ , respectively. The higher modulus of S50 and S65 imparts better resistance to subsurface crack propagation and, therefore, wear.

Sankarasubramanian et al.<sup>40</sup> found that two-dimensional filler particles, such as, clay or graphite nanoparticles imparted higher crack initiation resistance and crack propagation resistance to polymer composites than spherical carbon black particles. A flat filler particle will arrest crack growth if the direction of crack

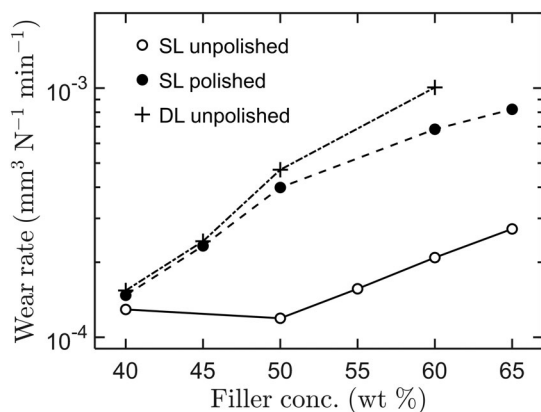


**FIGURE 14** Semilog plot of specific wear rate vs. filler concentration for the various PEEK/hBN/WC-CoCr composite coatings investigated in the present study

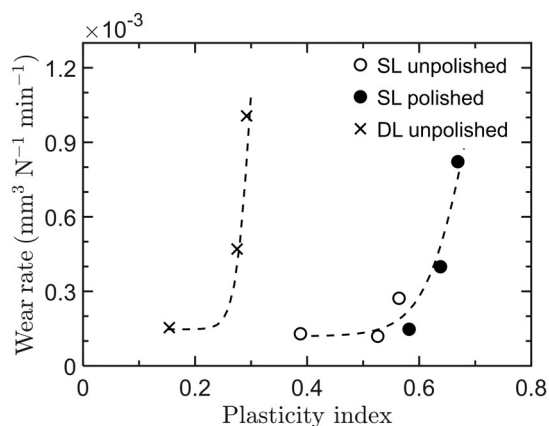


**FIGURE 15** Specific wear rate vs. plasticity index of single- and double-layered composite coatings

propagation is normal to the particle's flat surface. However, the lower wear resistance of D50 and D60 coatings (that have a higher concentration of two-dimensional hBN particles) is because the flat surfaces of hBN are aligned parallel to the surface (such alignment would be produced during the compression molding process) and parallel to the direction of crack propagation. The weak intermolecular forces between the hBN layers would allow separation of the layers and facilitate crack propagation through the hBN interlayers, which would cause an increase in the wear rate. The low friction coefficient of the double-layered coatings of the present study is attributed to this low shear strength.

The wear rate of the polished single-layered coating was found to be much higher than the wear rate of the corresponding unpolished coating of the same composition (cf. Figure 14). Pouzada et al.<sup>47</sup> reported that a large decrease in surface roughness because of polishing could lead to an increase in adhesion forces between the sliding surfaces that could increase friction (and wear). However, data in Figure 13(a) show that the friction coefficients decreased after polishing. The softer PEEK material is selectively removed during the polishing process, weakening the adhesive filler-polymer bonding at the surface, and facilitating the removal of the exposed filler particles.

The specific wear rate increased sharply with an increase in the coating's plasticity index beyond a critical value. This critical value can be seen in Figure 15 to be about 0.6 for the single-layered coatings and about 0.2 for the double-layered coatings.

## 5 | CONCLUSIONS

A mixed filler coating consisting of both hBN and WC-CoCr exhibited significantly improved properties

compared with PEEK-hBN composites previously reported in the literature. Coatings with room temperature modulus as high as 17 GPa, hardness as high as 0.7 GPa, and the friction coefficient as low as 0.21 were obtained. Ball milling the hBN, WC-CoCr, and PEEK particles for size reduction, and more importantly, for uniform blending of the three components, was essential for mechanical and tribological property enhancements.

Nanoindentation measurements using a sharp Berkovich indenter showed relatively broad distributions of reduced modulus and hardness values, attributed to the variation in local surface composition of the composite on the nanoscale. Measurements on unfilled PEEK coatings also showed a distribution in  $E_r$  and hardness values, attributed to the presence of amorphous and crystalline domains of the semicrystalline polymer at the surface. Only the polished surface of the unfilled PEEK coating exhibited a fairly narrow distribution of  $E_r$  and hardness. Mechanical polishing evidently results in the crystallization of the amorphous domains by the shear-induced alignment of the polymer chains.

In the case of single-layered coatings, the average  $E_r$  and average hardness showed a clear increase with an increase in the filler concentration in the composite. The average  $E_r$  and the average hardness could be correlated well with the total volume fraction of hBN and WC-CoCr in the composite. The calculated values of the microstructural parameter,  $J$ , indicated a continuity of the hard and soft phases. Double-layered coatings that contained only hBN in the top layer did not show an increase in average  $E_r$  or hardness with an increase in the filler concentration. In fact, the average  $E_r$  was lower for the double-layered coating containing 40 wt% of hBN in the top layer, compared with unfilled PEEK, which is attributed to a decrease in the crystallinity of PEEK because of the hBN particles.

For all the composite coatings, the plasticity index showed a logarithmic increase with an increase in the coating modulus. The specific wear rate increased with an increase in the plasticity index of the composite coating.

## ACKNOWLEDGMENTS


Financial support from General Electric Oil & Gas and the Center for Advanced Materials Processing at Clarkson University is gratefully acknowledged. The assistance of Aswin Pitchiya and Hubert Bilan in scanning electron microscopy of the composite powders is greatly appreciated.

## DATA AVAILABILITY STATEMENT

The data that support the findings of this study are openly available in figshare at <https://doi.org/10.6084/m9.figshare.13488222.v1>.

## ORCID

Janice L. Lebga-Nebane  <https://orcid.org/0000-0002-9544-6771>

Malavarayan Sankarasubramanian  <https://orcid.org/0000-0002-5668-6385>

Gregory Chojecki  <https://orcid.org/0000-0001-7732-8272>

Sitaraman Krishnan  <https://orcid.org/0000-0002-1228-8393>

## REFERENCES

- [1] B. Venkatesh, K. Sriker, V. S. V. Prabhakar, *Procedia Mater. Sci.* **2015**, *10*, 527. <https://doi.org/10.1016/j.mspro.2015.06.002>.
- [2] H. S. Klapper, N. S. Zadorozne, R. B. Rebak, *Acta Metallurgica Sinica* **2017**, *30*(4), 296. <https://doi.org/10.1007/s40195-017-0553-z>.
- [3] S. Delfani-Abbariki, A. Abdollah-zadeh, S. M. M. Hadavi, M. Abedi, S. M. R. Derakhshandeh, *Surf. Coat. Technol.* **2018**, *350*, 74. <https://doi.org/10.1016/j.surfcoat.2018.06.055>.
- [4] G. Tatsumi, M. Ratoi, Y. Shitara, K. Sakamoto, B. G. Mellor, *Tribol. Int.* **2020**, *151*, 106513. <https://doi.org/10.1016/j.triboint.2020.106513>.
- [5] Y. Yan, Z. Meng, H. Liu, J. Wang, B. Chen, F. Yan, *Tribol. Int.* **2020**, *144*, 106117. <https://doi.org/10.1016/j.triboint.2019.106117>.
- [6] D. P. Jones, D. C. Leach, D. R. Moore, *Polymer* **1985**, *26*(9), 1385. [https://doi.org/10.1016/0032-3861\(85\)90316-7](https://doi.org/10.1016/0032-3861(85)90316-7).
- [7] R. Goyal, A. Tiwari, Y. Negi, *Mater. Sci. Eng., A* **2008**, *486*(1), 602. <https://doi.org/10.1016/j.msea.2007.09.047>.
- [8] R. K. Goyal, A. N. Tiwari, Y. S. Negi, *Mater. Sci. Eng., A* **2008**, *491*(1–2), 230. <https://doi.org/10.1016/j.msea.2008.01.091>.
- [9] G. Zhang, A. K. Schlarb, S. Tria, O. Elkedim, *Compos. Sci. Technol.* **2008**, *68*(15–16), 3073. <https://doi.org/10.1016/j.compscitech.2008.06.027>.
- [10] R. K. Goyal, A. N. Tiwari, U. P. Mulik, Y. S. Negi, *J. Appl. Polym. Sci.* **2007**, *104*(1), 568. <https://doi.org/10.1002/app.25607>.
- [11] M. C. Kuo, C. M. Tsai, J. C. Huang, M. Chen, *Mater. Chem. Phys.* **2005**, *90*(1), 185. <https://doi.org/10.1016/j.matchemphys.2004.10.009>.
- [12] Q. Wang, Q. Xue, H. Liu, W. Shen, J. Xu, *Wear* **1996**, *198*(1), 216. [https://doi.org/10.1016/0043-1648\(96\)07201-8](https://doi.org/10.1016/0043-1648(96)07201-8).
- [13] D. Kumar, T. Rajmohan, S. Venkatachalapathi, *Mater. Today: Proc.* **2018**, *5*(6, Part 2), 14583. <https://doi.org/10.1016/j.matpr.2018.03.049>.
- [14] B. J. Briscoe, Y. Lin Heng, T. A. Stolarski, *Wear* **1986**, *108*(4), 357. [https://doi.org/10.1016/0043-1648\(86\)90013-X](https://doi.org/10.1016/0043-1648(86)90013-X).
- [15] Lebga, J. L. Mechanical and tribological properties of hexagonal boron nitride and tungsten carbide cobalt chrome filled polyetheretherketone nanocomposite coatings. Ph.D. Dissertation, Clarkson University, **2015**.
- [16] J. Tharajak, T. P. Narongrit, *Adv. Mater. Res.* **2011**, *410*, 333. <https://doi.org/10.4028/www.scientific.net/AMR.410.333>.
- [17] J. Tharajak, T. Palathai, N. Sombatsompop, *Surf. Coat. Technol.* **2015**, *273*, 20. <https://doi.org/10.1016/j.surfcoat.2015.03.030>.
- [18] J. Tharajak, T. Palathai, N. Sombatsompop, *Wear* **2017**, *372–373*, 68. <https://doi.org/10.1016/j.wear.2016.11.021>.
- [19] L. Liu, L. Xiao, M. Li, X. Zhang, Y. Chang, L. Shang, Y. Ao, *Colloid Polym. Sci.* **2016**, *294*(1), 127. <https://doi.org/10.1007/s00396-015-3733-2>.
- [20] Q. Wang, J. Xu, W. Shen, W. Liu, *Wear* **1996**, *196*(1–2), 82. [https://doi.org/10.1016/0043-1648\(95\)06866-x](https://doi.org/10.1016/0043-1648(95)06866-x).
- [21] W. C. Oliver, G. M. Pharr, *J. Mater. Res.* **1992**, *7*(6), 1564. <https://doi.org/10.1557/JMR.1992.1564>.
- [22] A. Sreeram, N. G. Patel, R. I. Venkatanarayanan, J. B. McLaughlin, S. J. DeLuca, P. A. Yuya, S. Krishnan, *Polym. Test.* **2014**, *37*, 86. <https://doi.org/10.1016/j.polymertesting.2014.04.012>.
- [23] J. F. Archard, *J. Appl. Phys.* **1953**, *24*(8), 981. <https://doi.org/10.1063/1.1721448>.
- [24] G. Z. Voyiadjis, A. Samadi-Dooki, L. Malekmotiei, *Polym. Test.* **2017**, *61*, 57. <https://doi.org/10.1016/j.polymertesting.2017.05.005>.
- [25] P. C. Dawson, D. J. Blundell, *Polymer* **1980**, *21*(5), 577. [https://doi.org/10.1016/0032-3861\(80\)90228-1](https://doi.org/10.1016/0032-3861(80)90228-1).
- [26] A. K. Kadiyala, J. Bijwe, P. Kalappa, *Surf. Coat. Technol.* **2018**, *334*, 124. <https://doi.org/10.1016/j.surfcoat.2017.11.026>.
- [27] M. Hedayati, M. Salehi, R. Bagheri, M. Panjepour, A. Maghizian, *Powder Technol.* **2011**, *207*(1–3), 296. <https://doi.org/10.1016/j.powtec.2010.11.011>.
- [28] R. T. Paine, C. K. Narula, *Chem. Rev.* **1990**, *90*(1), 73. <https://doi.org/10.1021/cr00099a004>.
- [29] V. Bonache, E. Rayón, M. D. Salvador, D. Busquets, *Mater. Sci. Eng., A* **2010**, *527*(12), 2935. <https://doi.org/10.1016/j.msea.2010.01.026>.
- [30] L. R. Pattison, A. Hexemer, E. J. Kramer, S. Krishnan, P. M. Petroff, D. A. Fischer, *Macromolecules* **2006**, *39*(6), 2225. <https://doi.org/10.1021/ma0521912>.
- [31] I. M. Daniel, O. Ishai, *Engineering Mechanics of Composite Materials*, 2nd ed., Oxford university press, New York **2005**.
- [32] S. Ji, Q. Wang, B. Xia, D. Marcotte, *J. Struct. Geol.* **2004**, *26*(8), 1377. <https://doi.org/10.1016/j.jsg.2003.12.004>.
- [33] B. J. Briscoe, L. Fiori, E. Pelillo, *J. Phys. D: Appl. Phys.* **1998**, *31*(19), 2395. <https://doi.org/10.1088/0022-3727/31/19/006>.
- [34] H. Shulha, A. Kovalev, N. Myshkin, V. V. Tsukruk, *Eur. Polym. J.* **2004**, *40*(5), 949. <https://doi.org/10.1016/j.eurpolymj.2004.01.021>.
- [35] A. Kovalev, H. Shulha, M. Lemieux, N. Myshkin, V. V. Tsukruk, *J. Mater. Res.* **2004**, *19*(3), 716. <https://doi.org/10.1557/jmr.2004.19.3.716>.
- [36] L. Wu, J. Jasinski, S. Krishnan, *J. Appl. Polym. Sci.* **2012**, *124*(3), 2154. <https://doi.org/10.1002/app.35233>.
- [37] N. Rathod, S. G. Hatzikiriakos, *Polym. Eng. Sci.* **2004**, *44*(8), 1543. <https://doi.org/10.1002/pen.20151>.
- [38] K. W. Stöckelhuber, A. Das, R. Jurk, G. Heinrich, *Polymer* **2010**, *51*(9), 1954. <https://doi.org/10.1016/j.polymer.2010.03.013>.
- [39] Y. Tsuji, Y. Kitamura, M. Someya, T. Takano, M. Yaginuma, K. Nakanishi, K. Yoshizawa, *ACS Omega* **2019**, *4*(3), 4491. <https://doi.org/10.1021/acsomega.9b00129>.
- [40] M. Sankarasubramanian, M. Torabizadeh, Z. A. Putnam, J. C. Moosbrugger, M. Y. Huang, S. Krishnan, *Polym. Test.* **2019**, *78*, 105932. <https://doi.org/10.1016/j.polymertesting.2019.105932>.
- [41] G. Zhang, H. Liao, H. Li, C. Mateus, J. M. Bordes, C. Coddet, *Wear* **2006**, *260*(6), 594. <https://doi.org/10.1016/j.wear.2005.03.017>.



- [42] K. A. Laux, A. Jean-Fulcrand, H. J. Sue, T. Bremner, J. S. S. Wong, *Polymer* **2016**, 103, 397. <https://doi.org/10.1016/j.polymer.2016.09.064>.
- [43] Z. Lu, K. Friedrich, B. Küntzler, *J. Synthetic Lubrication* **1995**, 12(2), 103. <https://doi.org/10.1002/jsl.3000120203>.
- [44] R. F. King, D. Tabor, *Proc. Phys. Soc. Section B* **1953**, 66(9), 728. <https://doi.org/10.1088/0370-1301/66/9/302>.
- [45] J. Ye, D. L. Burris, T. Xie, *Lubricants* **2016**, 4(1), 4. <https://doi.org/10.3390/lubricants4010004>.
- [46] T. A. Blanchet, F. E. Kennedy, *Wear* **1992**, 153(1), 229. [https://doi.org/10.1016/0043-1648\(92\)90271-9](https://doi.org/10.1016/0043-1648(92)90271-9).
- [47] A. S. Pouzada, E. C. Ferreira, A. J. Pontes, *Polym. Test.* **2006**, 25(8), 1017. <https://doi.org/10.1016/j.polymertesting.2006.06.009>.

## SUPPORTING INFORMATION

Additional supporting information may be found online in the Supporting Information section at the end of this article.

**How to cite this article:** Lebga-Nebane JL, Sankarasubramanian M, Chojecki G, et al. Polyetheretherketone, hexagonal boron nitride, and tungsten carbide cobalt chromium composite coatings: Mechanical and tribological properties. *J Appl Polym Sci.* 2021;e50504. <https://doi.org/10.1002/app.50504>

# Polyetheretherketone, hexagonal boron nitride, and tungsten carbide cobalt chromium composite coatings: mechanical and tribological properties

## Supporting Information

Janice L. Lebga-Nebane,<sup>a,e</sup> Malavarayan Sankarasubramanian,<sup>a,b,f</sup> Gregory Chojecki,<sup>a,b,g</sup> Bo Ning,<sup>c</sup> Philip A. Yuya,<sup>d</sup> John C. Moosbrugger,<sup>d</sup> Don H. Rasmussen,<sup>a</sup> Sitaraman Krishnan<sup>a,\*</sup>

<sup>a</sup> *Department of Chemical & Biomolecular Engineering, Clarkson University, Potsdam, NY, 13699, USA*

<sup>b</sup> *Materials Science & Engineering Ph.D. program, Clarkson University, Potsdam, NY, 13699, USA*

<sup>c</sup> *Oilfield Equipment Division, Baker Hughes, a GE Company, Houston, TX, 77086, USA*

<sup>d</sup> *Department of Mechanical & Aeronautical Engineering, Clarkson University, Potsdam, NY, 13699, USA*

<sup>e</sup> *Presently at Elinor Coatings, Fargo, ND 58102, USA*

<sup>f</sup> *Presently at Intel Corporation, Chandler, AZ, 85226, USA*

<sup>g</sup> *Presently at S-E-A Ltd., Columbus, OH, 43229, USA*

\*Corresponding author. E-mail address: [skrishna@clarkson.edu](mailto:skrishna@clarkson.edu)

## Scanning electron microscopy of as-received and processed powders of coating components

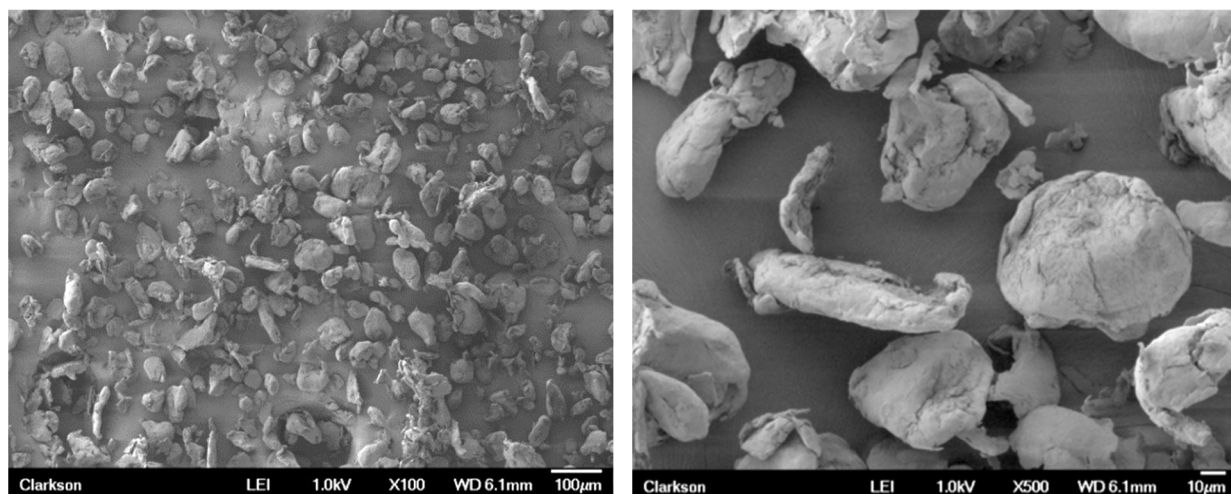


**FIGURE S1** SEM images of PEEK powder before ball milling.

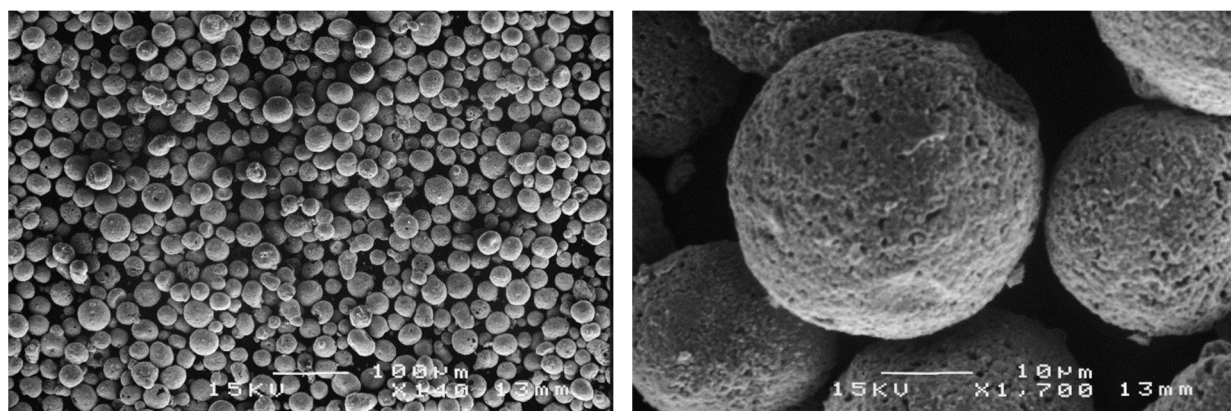


**FIGURE S2** SEM images of WC-CoCr powder before ball milling.

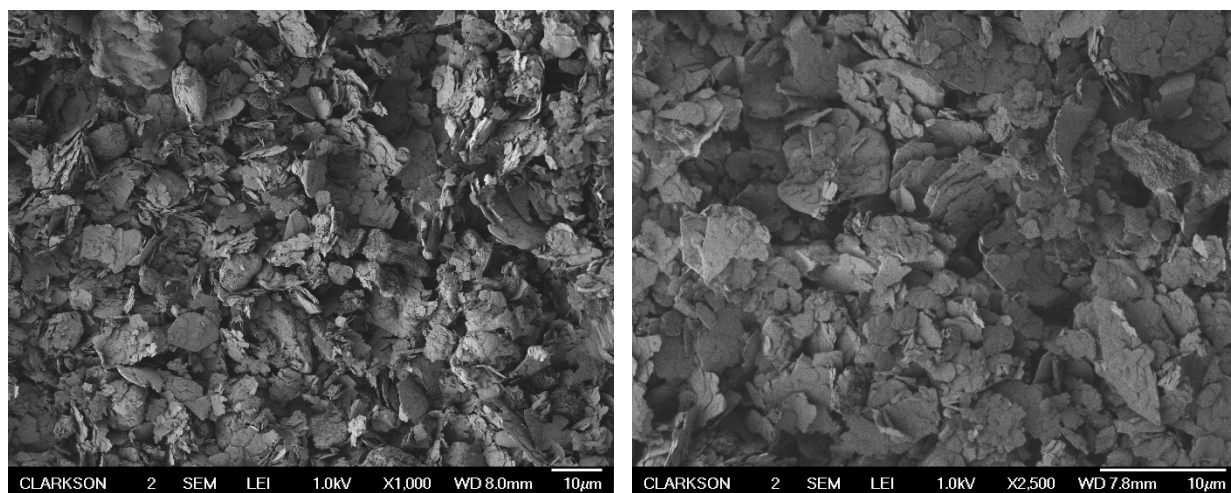


**FIGURE S3** SEM images of hBN powder before ball milling.



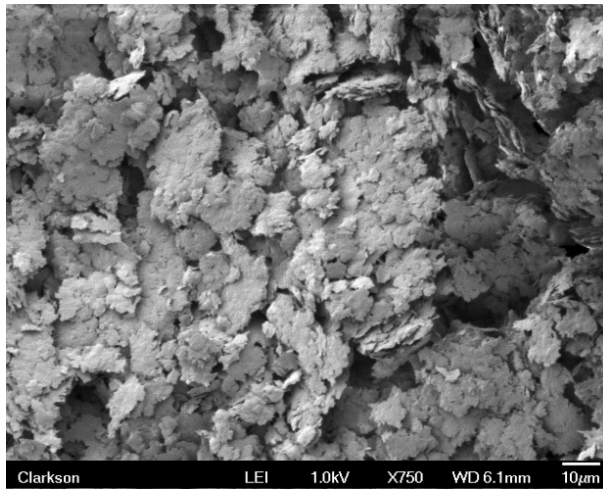


**FIGURE S4** SEM image of ball-milled PEEK. Ball milling resulted in a flattening of the as-received particles whose SEM images are shown in Fig. S1.



**FIGURE S5** (a) Photograph of a composite powder prepared by low-energy blending of PEEK (70 wt %) and hBN (30 wt %), and (b) its SEM image. The smaller particles are hBN, and the larger ones are flattened PEEK.

### **Procedure for the preparation of the composite coatings on the steel substrate**

The coatings were prepared by hot pressing the composite powders onto 2-mm thick 4130 alloy steel substrates using a Wabash compressor and a steel mold shown in Figs. 1(c) and 1(d). The steel substrates (5 cm × 5 cm) were polished using silicon carbide grinding discs (CarbiMet 2 S Abrasive Discs, P180 and P280 Grit) before coating them. A mold release agent (Mono-Coat E-7A, Chem-Trend, Howell, MI) was applied to the surface of the mold for easy detachment of the coated substrate after pressing. The mold temperature was increased from ambient to 400 °C over 30 min and held at this value for

1 h under a load of 4,500 kgf (applied over a mold contact area of 20 cm  $\times$  20 cm). The heating was stopped, and the load increased to 22,700 kgf. Cooling to room temperature occurred under this load. Fig. 1(e) shows a photograph of a steel substrate coated with the composite powder.

Two types of coatings were studied: single-layered and double-layered structures. For preparing the double-layered coatings, a weighed amount of the powder of the desired bottom-layer composition (consisting of PEEK and WC-CoCr) was placed on the steel substrate placed within the mold and compacted at room temperature under a load of 4 500 kgf, cyclically loading and unloading 3 times to achieve uniform coverage of the substrate. Then, the powder of the desired top-layer composition (consisting of PEEK and hBN) was applied uniformly on the compact bottom layer by the cyclic loading and unloading used to prepare the bottom layer. The assembled double-layered green compact was then hot pressed at 400 °C using the procedure described for the single-layered coatings. In Table S1, the sample names of single-layered coatings are prefixed with “S” and those of the double-layered coatings with “D”. The numbers in the sample names indicate the wt % of hBN and/or WC-CoCr.

The effects of surface roughness on the tribological properties of the coatings were investigated. The coatings were polished first using a water-based polycrystalline diamond suspension containing particles of 0.5  $\mu$ m size (Allied High Tech Products Inc, Rancho Dominguez, CA) and a Billiard polishing cloth, and then with an aqueous dispersion of alumina particles of 0.05  $\mu$ m diameter and a synthetic rayon cloth (MicroCloth, Buehler, Lake Bluff, IL). A Buehler Eco-Met III polisher (Buehler, Lake Bluff, IL) was used.

Polishing was accomplished in a two-step process. During the initial polishing step, the Billiard polishing cloth was mounted on the polisher’s platen and wetted with water. The diamond suspension was applied to the cloth, and the platen speed was set to the maximum level. The substrate to be polished was held in contact with the polishing cloth on the rotating platen and slowly reciprocated manually between the center and the edge of the cloth. The cloth was kept lubricated by applying water and diamond suspension

throughout the process. This step was carried out for about 20 min, followed by rinsing the substrate thoroughly in water. For the final polishing step, the Billiard cloth was replaced by MicroCloth, and the alumina slurry was used instead of the diamond slurry. Polishing using the alumina slurry was carried out for about ten minutes. All samples were thoroughly washed with water after polishing to remove any traces of slurry on the surface.

### Coating composition

Table S1 gives the volume fractions of PEEK, hBN, and WC-CoCr in the different coatings used in the correlations. The volume fractions were calculated using Eq. (9) in the main article, using the densities of PEEK, hBN, and WC-CoCr.

**TABLE S1** Concentrations, in volume percent, of PEEK, hBN, and WC-CoCr in powders used to prepare the single-layered and double-layered composite coatings.

	Volume percent		
	PEEK	hBN	WC-CoCr
<b>Single-layered coatings</b>			
S40	80.6	16.9	2.6
S50	73.4	23.1	3.5
S65	59.8	34.9	5.3
<b>Double-layered coatings, the top layer</b>			
D40	70.5	29.5	0.0
D50	61.4	38.6	0.0
D60	51.5	48.5	0.0
<b>Double-layered coatings, the bottom layer</b>			
D40	94.0	0.0	6.0
D50	91.3	0.0	8.7
D60	87.5	0.0	12.5



## Density of PEEK, hBN, and WC-CoCr

The density of PEEK ranges from about 1.265 to 1.40 g cm<sup>-3</sup> depending on the degree of crystallinity.<sup>1</sup> The manufacture specified density of 1.32 g cm<sup>-3</sup> (ISO 1183 test method) for VICOTE™ 701 PEEK was used in volume fraction calculations. The density of hBN is reported to be in the range of 2.0 to 2.28 g cm<sup>-3</sup>.<sup>2</sup> An average value of 2.1 g cm<sup>-3</sup> was used to calculate volume fractions in the present study. This value is close to the theoretical density,  $\rho$ , of 2.266 g cm<sup>-3</sup> found using:

$$\rho_{\text{hBN}} = \frac{n \sum_i A_i}{V_c N_A} \quad (\text{S.1})$$

where  $n$  is the number of atoms of boron and nitrogen per unit cell, equal to 2,  $\sum_i A_i$  is the sum of the atomic weights of the two elements ( $\cong 24.8$  g/mol),  $N_A$  is the Avogadro's number, and  $V_c$  is the unit cell volume given by:

$$V_c = \frac{3\sqrt{3}}{2} a^2 c \quad (\text{S.2})$$

where  $a$  and  $c$  are the lattice parameters of the hexagonal unit cell.  $a = 1.45$  Å and  $c = 6.66$  Å.<sup>3</sup>

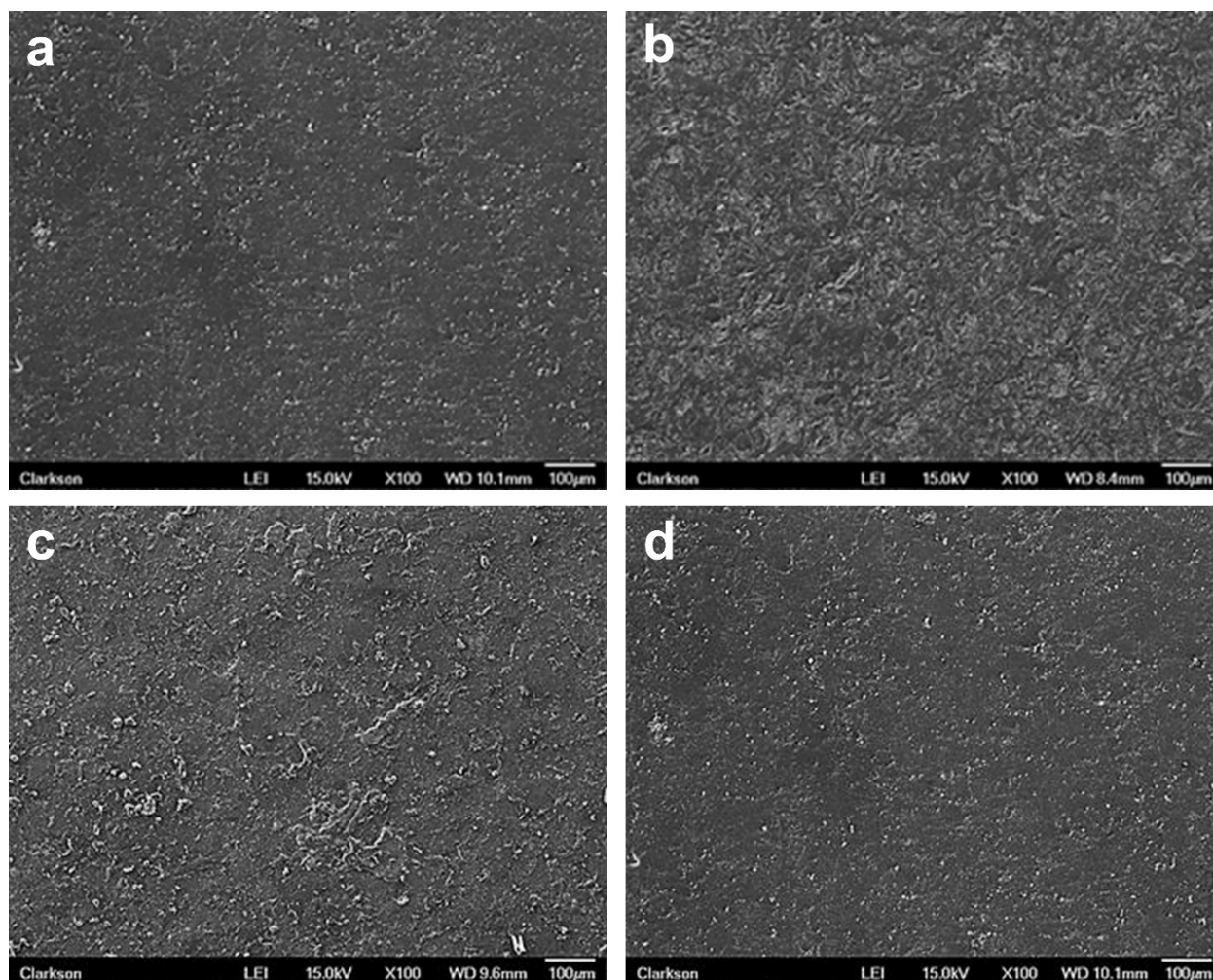
The supplier specified the WC-10Co-4Cr cermet particles used in the study to be of the fine carbide grain size type (with a grain size of a few micrometers). The particles' composition was approximately 79.8 wt % tungsten, 5 % carbon, 10.7 % Co, and 4.5 % Cr. The XRD peaks corresponding to WC-CoCr present in the as-received powder and the composite coatings (Fig. 4 of the main article) were consistent with other reports in the literature.<sup>4</sup> Several  $2\theta$  peaks characteristic of WC (HCP), at approximately 31.6°, 35.7°, 48.4°, 64.1°, 65.9°, 73.2°, 75.7°, and 77.7° attributed to reflections from the (0001), (10 $\bar{1}$ 0), (10 $\bar{1}$ 1), (2 $\bar{1}$  $\bar{1}$ 0), (0002), (2 $\bar{1}$  $\bar{1}$ 1), (20 $\bar{2}$ 0), and (10 $\bar{1}$ 2) crystallographic planes,<sup>5-6</sup> were observed (Fig. 4 of the main article). The peaks at 40.1°, 42.6°, and 46.6° are attributed to Co<sub>3</sub>W<sub>3</sub>C, and that at about 44° is attributed to the (111) reflection of FCC Co.<sup>7</sup>

WC-CoCr cermet particles are generally prepared by mechanical milling of WC, Co, and Cr powders with a binder [e.g., poly(ethylene glycol)] in water to obtain a stable

slurry.<sup>4</sup> The slurry is spray dried to obtain spherical agglomerates [cf. Fig. S2] that are heat-treated in a hydrogen atmosphere to consolidate and increase the agglomerates' cohesive strength. The resulting particles contain ternary cubic carbide phases such as  $\text{Co}_3\text{W}_3\text{C}$ , as reported by others,<sup>8</sup> and observed in the X-ray diffraction patterns of the present study. However, for the estimation of the average density of the cermet, the presence of only WC, Co, and Cr, with respective densities of 15.63, 8.90, and 7.19 g cm<sup>-3</sup> was assumed, and the average density was found to be 13.8 g cm<sup>-3</sup> using Eq. (8) in the main article that is based on the reasonable assumption that the total volume of the composite particle is equal to the sum of the volumes of the individual components. The estimated density of 13.8 g cm<sup>-3</sup> is in reasonable agreement with the density of 13.7 g cm<sup>-3</sup> determined by Bolleli et al.<sup>9</sup> for a coating with a porosity of 1.1 vol %, prepared using the high-velocity oxy-fuel spray process. In contrast with coatings prepared by thermal-spray methods, the compression-molded coatings of the present study that contain a polymeric binder (PEEK) would be of significantly lower porosity.

### **Scanning electron microscopy analysis of the coating surfaces**

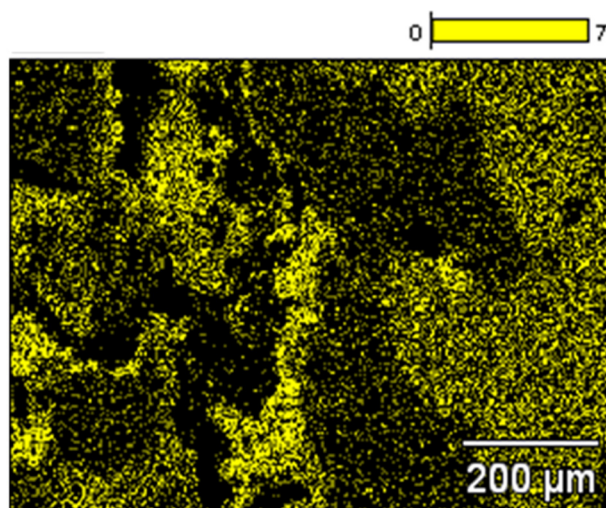
Fig. S6 shows SEM images of the surfaces of some single- and double-layered coatings. Compact films with a moderate degree of surface roughness are observed.



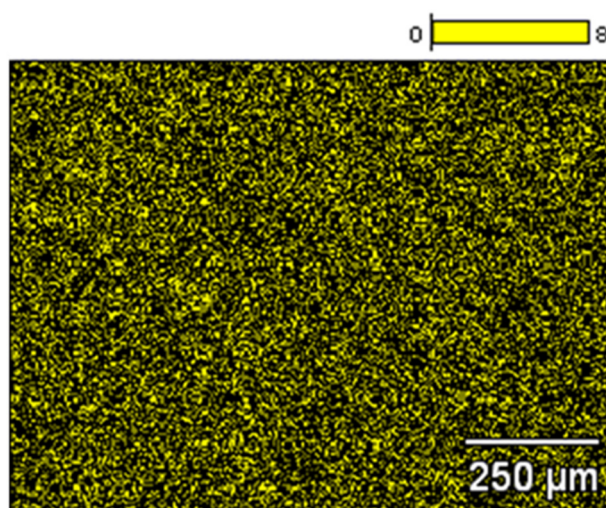
**FIGURE S6** SEM images of the single-layered coatings (a ) S40, (b) S50, and (c) S60, and the double-layered coating D40.

*Effect of ball-milling on the dispersion of filler particles in the polymer matrix.* A set of composite powders were prepared by shaking a mixture of the dry powders of the different components in a capped glass vial. The hand-mixed powders were not subjected to particle size reduction and homogenization in a ball mill. Ball-milled powders showed more uniform filler distribution within the polymer matrix.





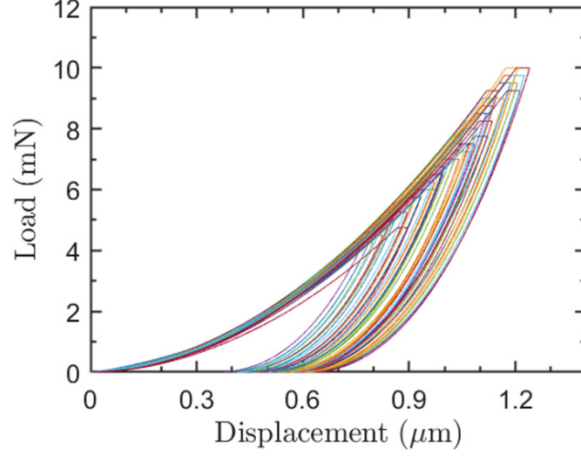
**FIGURE S7** Energy-dispersive X-ray spectroscopy of a coating (60 wt % PEEK, 20 wt % hBN, and 20 wt % WC-CoCr) showing the distribution of hBN at the surface of a coating obtained from as-received composite powders. The bright spots correspond to regions with high atomic concentrations of boron atoms from hBN. A non-uniform distribution of hBN particles can be inferred.



**FIGURE S8** Energy-dispersive X-ray spectroscopy of a coating (60 wt % PEEK, 20 wt % hBN, and 20 wt % WC-CoCr) showing the uniform distribution of hBN at the surface of a coating prepared using a ball-milled composite powder.

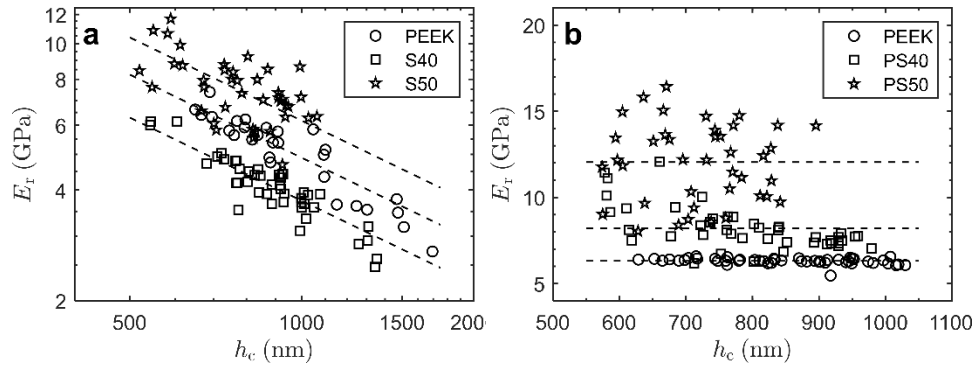
## Nanoindentation analysis

Fig. S9 shows the load-displacement curves from room temperature nanoindentation measurements on a polished PEEK coating.



**FIGURE S9** Load-displacement curves from nanoindentation measurements on polished PEEK coating.

Decreasing the surface roughness of the coatings by polishing showed an interesting effect on the variation of  $E_r$  with contact depth,  $h_c$ . For a given surface, the contact depth varied in our experiments not only because of the variation in the maximum applied load,  $P_{\max}$ , but also because the maximum indentation depth,  $h_{\max}$ , generally increased with an increase in  $P_{\max}$  [cf. Eq. (4)]. As seen in Fig. S10(a), the rougher unpolished surfaces showed an anomalous power-law dependence of  $E_r$  on  $h_c$ . The order of dependence of  $E_r$  on  $h_c$  was approximately  $-0.75$  for the coatings shown in Fig. 9(a) of the main article. In contrast, the polished coatings showed no correlation between  $E_r$  and  $h_c$  (as expected).



**FIGURE S10** Variation of reduced modulus of (a) unpolished and (b) polished coatings with contact depth in nanoindentation.

Because the projected contact area in nanoindentation analysis is calculated as a function of the indentation depth into the sample, the surface roughness, which is characterized by the spatial distribution and height of asperities across the surface, introduces errors in the calculation of the contact area and subsequently in the hardness and reduced modulus results.<sup>10-13</sup> Tabor<sup>14</sup> noted that indenting at depths greater than the surface asperities, as in the experiments of the present study, significantly reduced the effects of surface roughness on hardness. Furthermore, polishing the coating is an effective method of reducing the impact of surface roughness.<sup>15</sup> Since the samples for nanoindentation tests had a thickness in the range of 200–500  $\mu\text{m}$  and the maximum indentation depth was less than 2  $\mu\text{m}$ , the steel substrate does not influence the reported results.

## Mechanics of materials models

*Correlation of the composite modulus with the modulus of the individual components*

*Cubic filler models.* The models of Paul,<sup>16</sup> and Ishai and Cohen,<sup>17</sup> assume cubic reinforcing filler particles and result in the Eqs. (S.3) and (S.4), respectively, for the elastic modulus of a binary composite of the filler and the matrix.

$$E_c^{[\text{Paul}]} = E_m \left[ \frac{1 + (m - 1)\phi_f^{2/3}}{1 + (m - 1)(\phi_f^{2/3} - \phi_f)} \right] \quad (\text{S.3})$$

$$E_c^{[\text{Ishai-Cohen}]} = E_m \left[ 1 + \frac{\phi_f}{m/(m - 1) - \phi_f^{1/3}} \right] \quad (\text{S.4})$$

where  $m$  is the ratio of the elastic modulus of filler to that of the matrix,  $E_m$  is the modulus of the matrix, and  $\phi_f$  is the volume fraction of the reinforcing filler.

*Halpin–Tsai model.* According to the Halpin–Tsai relations<sup>18-19</sup> the general composite property,  $P_c$ , is obtained as

$$P_c = \frac{P_m(1 + \xi\eta\phi_f)}{1 - \eta\phi_f} \quad (\text{S.5})$$



where

$$\eta = \frac{P_f - P_m}{P_f + \xi P_m} \quad (\text{S.6})$$

$P_f$  and  $P_m$  are the filler and matrix properties, and  $\xi$  is a model parameter called the reinforcing efficiency.  $\xi \rightarrow \infty$  leads to the Voigt model, and  $\xi = 0$  leads to the Reuss model.

### PEEK, hBN, and WC-CoCr properties

Table S2 gives selected physical properties of PEEK, hBN, and WC-CoCr.

**TABLE S2** Physical properties of individual components of the composites at room temperature.

	PEEK	hBN	WC-CoCr
Density (g/cm <sup>3</sup> )	1.32	2.1	13.8
Hardness (GPa)	0.39 ± 0.02	0.20 ± 0.05	30
Modulus (GPa)	6.3 ± 0.2	20 ± 2	590

The glass transition and melting temperatures of PEEK (differential scanning calorimetry results provided by the supplier) were 143 °C and 343 °C, respectively. The hardness and modulus values of PEEK are measurements on the polished PEEK coatings of the present study. The values reported in Table S2 were used for the composition–property analysis of all the coatings, regardless of the degree of crystallinity of PEEK in them. Vickers hardness of hBN specimens, prepared by reactive hot-pressing of hBN powder at 1900 °C and 50 MPa in the presence of B<sub>2</sub>O<sub>3</sub> as a sintering additive, has been reported to be in the range of 0.15 to 0.25 GPa.<sup>20</sup> Young’s modulus of two-dimensional hBN sheets, calculated using molecular dynamics simulations, is found to be 790 ± 50 GPa.<sup>21</sup> However, the bulk modulus value of 20 ± 2 GPa, calculated by Fuchizaki et al.<sup>22</sup> using X-ray diffraction data, is expected to be more representative of the hBN particles in the coatings of the present study. The hardness and modulus values of WC-CoCr are estimated using the nanoindentation data of Bonache et al.<sup>8</sup>

*Modulus of WC-CoCr cermet.* Ravichandran<sup>23</sup> found the Young's modulus of WC-Co cermets of various compositions to be in the range of 440 GPa to 672 GPa and showing good correlation with the properties of WC and Co phases (assumed to be the only two phases present) based on Paul's model.

Bonache et al.,<sup>8</sup> however, observed at least three distinct microphases with widely different mechanical properties in their nanoindentation study of the WC-12Co cermet. These phases were cobalt matrix, tungsten carbide, and the ternary cubic carbide  $\eta$  phase ( $\text{Co}_3\text{W}_3\text{C}/\text{Co}_6\text{W}_6\text{C}$ ). Because of the considerable variation in microphase properties, an estimation of an average hardness or modulus of the composite using the individual microphases' properties is challenging, especially without knowing the relative volumes of these phases.

Nevertheless, assuming that WC and Co are the only dominant phases in the cermet (in accordance with Ravichandran<sup>23</sup>) with volume fractions of 0.8 and 0.2, respectively, and that the modulus of the WC and Co phases are  $E_{\text{WC}} = 717$  GPa and  $E_{\text{Co}} = 240$  GPa, respectively,<sup>23</sup> Paul's model predicted Young's modulus of the composite to be about 580 GPa. This estimate did not include the contribution of Cr, whose concentration in the cermet was small relative to WC or Co. The model of Ji et al.<sup>24</sup> predicted a modulus value of about 590 GPa, which is fairly close to the one obtained using Paul's model. The hardness of the composite was similarly estimated to be about 30 GPa, using the hardness of the WC and Co phases to be  $H_{\text{WC}} = 40$  GPa and  $H_{\text{Co}} = 8$  GPa, respectively.

### **Modulus of PEEK/hBN/WC-CoCr Composites**

Using the reduced modulus of PEEK determined using nanoindentation ( $\cong 6.3$  GPa) as  $E_{\text{m}}$  and the total volume fraction of the filler particles,  $\phi_{\text{f}}$ , equal to the sum of the volume fractions of hBN and WC-CoCr coatings in the coatings ( $\phi_{\text{f},1} + \phi_{\text{f},2} = 1 - \phi_{\text{p}}$ ), the ratio  $m$  of the effective modulus of the binary mixture of the filler particles to the modulus of the PEEK matrix can be determined by fitting the experimentally determined  $E_{\text{r}}$  values of the composite coatings to the two different models.

For Paul’s model,  $m$  was found using non-linear least-squares data fitting to be  $2.0 \pm 0.4$ . The predicted values of the PEEK/hBN/WC-CoCr composite modulus, using this  $m$ , are shown in the last column of Table S3.

**TABLE S3** Reduced modulus of polished single-layered coatings of different compositions measured using nanoindentation and comparison with the prediction of Paul’s model.

	$\phi_p$ (PEEK)	$\phi_{f,1}$ (hBN)	$\phi_{f,2}$ (WC-CoCr)	Measured $E_r$ (GPa)	Paul model prediction (GPa) <sup>a</sup>
PS40	0.806	0.169	0.026	$8.11 \pm 1.09$	10.52
PS50	0.734	0.231	0.035	$12.1 \pm 2.23$	12.26
PS65	0.598	0.349	0.053	$17.3 \pm 3.19$	16.53

<sup>a</sup> Fit parameter,  $m = 2.0$

Because  $m$  is the ratio of the effective elastic modulus of the combined filler particles (hBN and WC-CoCr) to the elastic modulus of PEEK,  $m = 2.0 \pm 0.4$  implies that the effective modulus of the mixed-filler is  $(13 \pm 3)$  GPa, which is significantly lower than expected based on the individual elastic modulus values of the two fillers. As discussed in the main article, the elastic modulus of hBN,  $E_{f,1}$ , is  $\cong 20$  GPa, and that of WC-CoCr,  $E_{f,2}$ , is  $\cong 590$  GPa. Using the relative volumes of the two fillers in the mixture (86.8 vol % hBN and 13.2 vol % of WC-CoCr), the lower and upper bounds of this filler mixture’s modulus are expected to be about 22.9 GPa and 95.3 GPa, respectively. The Ishai–Cohen model, similarly, did not result in a practical value of  $m$ . In contrast with the Paul model that gave a far too low value of  $m$ , the Ishai-Cohen model predicted a value that was far too high ( $\sim 10^8$ ). Thus, neither of these models is appropriate for the fitting of the modulus values of the present system.

### Surface energy of PEEK

The surface energy of PEEK was calculated using the contact angles of probe liquids such as water, formamide, and diiodomethane on PEEK, reported previously,<sup>25-26</sup> and using

the Owens–Wendt–Kaelble (OWK) method as described by Krishnan and coworkers.<sup>27</sup> The dispersion and polar components of the surface energy of the polymer were obtained by solving

$$\frac{\gamma_{L,i}(1 + \cos \theta_i)}{2} = \sqrt{\gamma_{L,i}^d} \sqrt{\gamma_S^d} + \sqrt{\gamma_{L,i}^p} \sqrt{\gamma_S^p} \quad (\text{S.7})$$

using the contact angle,  $\theta_i$  of the probe liquid,  $i$ , on the polymer surface, the total surface energy,  $\gamma_{L,i}$ , of the probe liquid, and its dispersion component,  $\gamma_{L,i}^d$ , and the polar component,  $\gamma_{L,i}^p$ , of surface energy. In matrix form, this equation can be written as:<sup>27</sup>

$$\mathbf{y} = \mathbf{X}\boldsymbol{\beta} \quad (\text{S.8})$$

where

$$\mathbf{y} = \begin{bmatrix} \gamma_{L,1}(1 + \cos \theta_1)/2 \\ \gamma_{L,2}(1 + \cos \theta_2)/2 \\ \gamma_{L,3}(1 + \cos \theta_3)/2 \end{bmatrix}, \mathbf{X} = \begin{bmatrix} \sqrt{\gamma_{L,1}^d} & \sqrt{\gamma_{L,1}^p} \\ \sqrt{\gamma_{L,2}^d} & \sqrt{\gamma_{L,2}^p} \\ \sqrt{\gamma_{L,3}^d} & \sqrt{\gamma_{L,3}^p} \end{bmatrix}, \text{ and } \boldsymbol{\beta} = \begin{bmatrix} \sqrt{\gamma_S^d} \\ \sqrt{\gamma_S^p} \end{bmatrix}. \text{ The solution of Eq. (S.8) is:}$$

$$\boldsymbol{\beta} = (\mathbf{X}^T \mathbf{X})^{-1} \mathbf{X}^T \mathbf{y} \quad (\text{S.9})$$

Table S4 gives the contact angle data from the literature, and Table S5 gives the surface energy components of the probe liquids. The contact angles for a given liquid varied significantly between the reported studies.

**TABLE S4** Contact angle of the probe liquids on PEEK;  $\theta_a$  is the advancing contact angle and  $\theta_r$  is the receding contact angle.

Liquid	Rymuszka et al. <sup>26</sup>		Terpiłowski et al. <sup>25</sup>		Wilson et al. <sup>28</sup>
	$\theta_a$	$\theta_r$	$\theta_a$	$\theta_r$	
Water	83°	69°	73°	61°	85°
Formamide	67°	58°	40°	33°	-
Diiodomethane	33°	23°	19°	13°	32°



The surface energy of PEEK was calculated using the two sets of surface energy parameters available in the literature for the probe liquids (Table S5), using the advancing contact angle,  $\theta_a$ , the receding contact angle,  $\theta_r$ , and the average contact angle,  $\bar{\theta}$ , defined as:

$$\bar{\theta} = \cos^{-1} \left( \frac{\cos \theta_a + \cos \theta_r}{2} \right) \quad (\text{S.10})$$

and these values are shown in Tables S6 and S7 for the contact angles reported by Rymuszka et al.<sup>26</sup> and Terpiłowski et al.,<sup>25</sup> respectively. The numbers in the parentheses are the statistical uncertainties in the reported values, estimated using our previously reported procedure.<sup>27</sup>

**TABLE S5** Surface energy parameters (in mJ m<sup>-2</sup>) of the probe liquids at room temperature.

	Fowkes et al. <sup>29</sup>			Smith and Pitrola <sup>30</sup>		
	Water	Formamid e	Diiodomethan e	Water	Formamid e	Diiodomethan e
$\gamma_S^d$	21.1	28.0	50.8	21.8	39.5	48.5
$\gamma_S^p$	52.3	29.3	0	51.0	18.7	2.3
$\gamma_s$	72.4	57.3	50.8	72.8	58.2	50.8

**TABLE S6** Surface energy parameters (in mJ m<sup>-2</sup>) of PEEK determined using the contact angle data of Rymuszka et al.<sup>26</sup> and surface energy parameters of Fowkes et al.<sup>29</sup> and Smith and Pitrola.<sup>30</sup>

	Fowkes et al.			Smith and Pitrola		
	With $\theta_a$	With $\theta_r$	With $\bar{\theta}$	With $\theta_a$	With $\theta_r$	With $\bar{\theta}$
$\gamma_S^d$	42 (4)	45 (8)	43 (6)	36 (9)	36 (12)	36 (10)
$\gamma_S^p$	2 (1)	5 (3)	3 (2)	2 (2)	7 (6)	4 (4)
$\gamma_s$	44 (5)	50 (11)	46 (8)	38 (11)	43 (18)	40 (14)

**TABLE S7** Surface energy parameters (in  $\text{mJ m}^{-2}$ ) of PEEK determined using the contact angle data of Terpiłowski et al.<sup>25</sup> and surface energy parameters of Fowkes et al.<sup>29</sup> and Smith and Pitrola.<sup>30</sup>

	Fowkes et al.			Smith and Pitrola		
	With $\theta_a$	With $\theta_r$	With $\bar{\theta}$	With $\theta_a$	With $\theta_r$	With $\bar{\theta}$
$\gamma_S^d$	49 (4)	49 (1)	49 (1)	43.6 (0.1)	41 (3)	42 (1)
$\gamma_S^p$	5 (1)	8.7 (0.5)	6.7 (0.6)	5.2 (0.1)	11 (2)	7.8 (0.7)
$\gamma_s$	54 (5)	58 (2)	56 (2)	48.8 (0.2)	52 (5)	50 (2)

Comparing the surface energy values based on the parameters of Fowkes et al. and Smith and Pitrola in Table S6, it is seen that the parameters of Fowkes et al. resulted in a better fit of the OWK model to the experimental data (note the smaller uncertainties in the estimated surface energy values). For the calculations using the average contact angle,  $\bar{\theta}$ ,  $\gamma_{\text{PEEK}}^d = 43 \pm 6 \text{ mJ m}^{-2}$  and  $\gamma_{\text{PEEK}}^p = 3 \pm 2 \text{ mJ m}^{-2}$  for the Fowkes et al. parameters and  $\gamma_{\text{PEEK}}^d = 36 \pm 10 \text{ mJ m}^{-2}$  and  $\gamma_{\text{PEEK}}^p = 4 \pm 4 \text{ mJ m}^{-2}$  for the Smith and Pitrola parameters.

The contact angle data of Terpiłowski et al. (Table S7) resulted in much better fits to the OWK model (uncertainties were significantly lower), but the calculated surface energy values were higher:  $\gamma_{\text{PEEK}}^d = 49 \pm 1 \text{ mJ m}^{-2}$  and  $\gamma_{\text{PEEK}}^p = 6.7 \pm 0.6 \text{ mJ m}^{-2}$  for the Fowkes et al. parameters and  $\gamma_{\text{PEEK}}^d = 42 \pm 1 \text{ mJ m}^{-2}$  and  $\gamma_{\text{PEEK}}^p = 7.8 \pm 0.7 \text{ mJ m}^{-2}$  for the Smith and Pitrola parameters.

Furthermore, these values compare favorably with the surface energy values reported by Wilson et al.<sup>28</sup> ( $\gamma_{\text{PEEK}}^d = 43.4 \text{ mJ m}^{-2}$  and  $\gamma_{\text{PEEK}}^p = 1.4 \text{ mJ m}^{-2}$ ) and Bhatnagar et al.<sup>31</sup> ( $\gamma_{\text{PEEK}}^d = 46.8 \text{ mJ m}^{-2}$  and  $\gamma_{\text{PEEK}}^p = 4.3 \text{ mJ m}^{-2}$ ), although their measurements were for a polyaryletheretherketone whose chemical structure is different from that of simple PEEK [poly(oxy-1,4-phenyleneoxy-1,4-phenylenecarbonyl-1,4-phenylene)]. In all cases, the polar component of PEEK surface energy is seen to be significantly lower than the dispersion component.

Based on the above analysis, the total surface energy of PEEK is expected to be in the range of  $48 \pm 8 \text{ mJ m}^{-2}$  with a dispersion component of  $43 \pm 5 \text{ mJ m}^{-2}$  and a polar component of  $5 \pm 3 \text{ mJ m}^{-2}$ .

## References

1. Dawson, P. C.; Blundell, D. J., X-ray data for poly(aryl ether ketones). *Polymer* **1980**, *21* (5), 577-578.
2. Rumyantsev, S. L.; Levinshtein, M. E.; Jackson, A. D.; Mohammad, S. N.; Harris, G. L.; Spencer, M. G.; Shur, M., Boron Nitride (BN). In *Properties of Advanced Semiconductor Materials: GaN, AlN, InN, BN, SiC, SiGe*, Levinshtein, M. E.; Rumyantsev, S. L.; Shur, M. S., Eds. John Wiley & Sons: 2001; pp 67-92.
3. Tsuji, Y.; Kitamura, Y.; Someya, M.; Takano, T.; Yaginuma, M.; Nakanishi, K.; Yoshizawa, K., Adhesion of epoxy resin with hexagonal boron nitride and graphite. *ACS Omega* **2019**, *4* (3), 4491-4504.
4. Wang, D.; Zhang, B.; Jia, C.; Gao, F.; Yu, Y.; Chu, K.; Zhang, M.; Zhao, X., Influence of carbide grain size and crystal characteristics on the microstructure and mechanical properties of HVOF-sprayed WC-CoCr coatings. *International Journal of Refractory Metals and Hard Materials* **2017**, *69*, 138-152.
5. Chakravarthy, G. V.; Chandran, M.; Bhattacharya, S. S.; Rao, M. S. R.; Kamaraj, M., A comparative study on wear behavior of TiN and diamond coated WC-Co substrates against hypereutectic Al-Si alloys. *Applied Surface Science* **2012**, *261*, 520-527.
6. Persson, K., Materials Data on WC (SG:187) by Materials Project. **2016**.
7. Persson, K., Materials Data on Co (SG:225) by Materials Project. **2014**.
8. Bonache, V.; Rayón, E.; Salvador, M. D.; Busquets, D., Nanoindentation study of WC-12Co hardmetals obtained from nanocrystalline powders: Evaluation of hardness and modulus on individual phases. *Materials Science and Engineering: A* **2010**, *527* (12), 2935-2941.

9. Bolelli, G.; Berger, L. M.; Börner, T.; Koivuluoto, H.; Lusvarghi, L.; Lyphout, C.; Markocsan, N.; Matikainen, V.; Nylén, P.; Sassatelli, P.; Trache, R.; Vuoristo, P., Tribology of HVOF- and HVAF-sprayed WC–10Co4Cr hardmetal coatings: A comparative assessment. *Surface and Coatings Technology* **2015**, *265*, 125-144.
10. Kim, J.-Y.; Lee, J.-J.; Lee, Y.-H.; Jang, J.-i.; Kwon, D., Surface roughness effect in instrumented indentation: A simple contact depth model and its verification. *Journal of Materials Research* **2006**, *21* (12), 2975-2978.
11. Jiang, W.-G.; Su, J.-J.; Feng, X.-Q., Effect of surface roughness on nanoindentation test of thin films. *Engineering Fracture Mechanics* **2008**, *75* (17), 4965-4972.
12. Walter, C.; Mitterer, C., 3D versus 2D finite element simulation of the effect of surface roughness on nanoindentation of hard coatings. *Surface and Coatings Technology* **2009**, *203* (20–21), 3286-3290.
13. Chen, L.; Ahadi, A.; Zhou, J.; Ståhl, J.-E., Modeling effect of surface roughness on nanoindentation tests. *Procedia CIRP* **2013**, *8* (0), 334-339.
14. Tabor, D., *The hardness of metals*. Oxford University Press: New York, 2000.
15. Fischer-Cripps, A. C., *Nanoindentation*. 3rd ed.; Springer-Verlag: New York, 2011; p xxi-xxii.
16. Paul, B., Prediction of elastic constants of multiphase materials. *Transactions of the Metallurgical Society of AIME* **1960**, *128*, 36-41.
17. Ishai, O.; Cohen, L. J., Elastic properties of filled and porous epoxy composites. *International Journal of Mechanical Sciences* **1967**, *9* (8), 539-546.
18. Halpin, J. C.; Kardos, J. L., The Halpin-Tsai equations: A review. *Polymer Engineering & Science* **1976**, *16* (5), 344-352.
19. Daniel, I. M.; Ishai, O., *Engineering Mechanics of Composite Materials*. 2nd ed.; Oxford University Press: New York, 2006.
20. Ertuğ, B., Powder preparation, properties and industrial applications of hexagonal boron nitride. In *Sintering Applications*, Ertuğ, B., Ed. Intech: Rijeka, Croatia, 2013; pp 33-55.



21. Thomas, S.; Ajith, K. M.; Valsakumar, M. C., Directional anisotropy, finite size effect and elastic properties of hexagonal boron nitride. *Journal of Physics: Condensed Matter* **2016**, *28* (29), 295302.
22. Fuchizaki, K.; Nakamichi, T.; Saitoh, H.; Katayama, Y., Equation of state of hexagonal boron nitride. *Solid State Communications* **2008**, *148* (9), 390-394.
23. Ravichandran, K. S., Fracture toughness of two-phase WC-Co cermets. *Acta Metallurgica et Materialia* **1994**, *42* (1), 143-150.
24. Ji, S.; Wang, Q.; Xia, B.; Marcotte, D., Mechanical properties of multiphase materials and rocks: a phenomenological approach using generalized means. *Journal of Structural Geology* **2004**, *26* (8), 1377-1390.
25. Terpiłowski, K.; Wiącek, A. E.; Jurak, M., Influence of nitrogen plasma treatment on the wettability of polyetheretherketone and deposited chitosan layers. *Advances in Polymer Technology* **2018**, *37* (6), 1557-1569.
26. Rymuszka, D.; Terpiłowski, K.; Borowski, P.; Holysz, L., Time-dependent changes of surface properties of polyether ether ketone caused by air plasma treatment. *Polymer International* **2016**, *65* (7), 827-834.
27. Wu, L.; Jasinski, J.; Krishnan, S., Carboxybetaine, sulfobetaine, and cationic block copolymer coatings: A comparison of the surface properties and anti-biofouling behavior. *Journal of Applied Polymer Science* **2012**, *124* (3), 2154-2170.
28. Wilson, A.; Jones, I.; Salamat-Zadeh, F.; Watts, J. F., Laser surface modification of poly(etheretherketone) to enhance surface free energy, wettability, and adhesion. *International Journal of Adhesion and Adhesives* **2015**, *62*, 69-77.
29. Fowkes, F. M.; Riddle, F. L.; Pastore, W. E.; Weber, A. A., Interfacial interactions between self-associated polar liquids and squalane used to test equations for solid-liquid interfacial interactions. *Colloids and Surfaces* **1990**, *43* (2), 367-387.
30. Smith, R.; Pitrola, R., Influence of casting substrate on the surface free energy of various polyesters. *Journal of Applied Polymer Science* **2002**, *83* (5), 997-1008.

31. Bhatnagar, N.; Jha, S.; Bhowmik, S.; Gupta, G.; Moon, J. B.; Kim, C. G., Physico-chemical characteristics of high-performance polymer modified by low and atmospheric pressure plasma. *Surface Engineering and Applied Electrochemistry* **2012**, *48* (2), 117-126.